NUREG/CR-1618
BNL-NUREG-51255
AN, R-1,4,5

WATER REACTOR SAFETY RESEARCH DIVISION

QUARTERLY PROGRESS REPORT
APRIL 1 - JUNE 30, 1980

HERBERT J.C. KOUTS, Department Chairman
WALTER Y. KATO, Deputy Chairman

Principal Investigators:

N. Abuaf
M.M. Levine
P. Saha
D. van Rooyen

Compiled by: Anthony J. Romano
Manuscript Completed: July 1980

DEPARTMENT OF NUCLEAR ENERGY
BROOKHAVEN NATIONAL LABORATORY, ASSOCIATED UNIVERSITIES, INC.
UPTON, NEW YORK 11973

Prepared for the
REACTOR SAFETY RESEARCH DIVISION
OFFICE OF NUCLEAR REGULATORY RESEARCH
U.S. NUCLEAR REGULATORY COMMISSION
Contract No. DE-AC02-76CH00016
FIN Nos.:

A-3014
A-3045
A-3208
A-3215

Available from
GPO Sales Program
Division of Technical Information and Document Control
U.S. Nuclear Regulatory Commission
Washington, D.C. 20555
and
National Technical Information Service
Springfield, Virginia 22161

FOREWORD

The Water Reactor Safety Research Programs Quarterly Report describes current activities and technical progress in the programs at Brookhaven National Laboratory sponsored by the USNRC Division of Reactor Safety Research. The projects reported each quarter are the following: LWR Thermal Hydraulic Development, Advanced Code Evaluation, TRAC Code Assessment, and Stress Corrosion Cracking of PWR Steam Generator Tubing.

The previous reports, BNL-NUREG-50624, BNL-NUREG-50661, BNL-NUREG-50683, BNL-NUREG-50747, BNL-NUREG-50785, BNL-NUREG-50820, BNL-NUREG-50883, BNL-NUREG-50931, BNL-NUREG-50978, BNL-NUREG-51015, BNL-NUREG-51081, BNL-NUREG-51131, BNL-NUREG-51178, and BNL-NUREG-51218 have covered the periods October 1, 1976 through March 31, 1980.

WATER REACTOR SAFETY RESEARCH

TABLE OF CONTENTS

I. LIGHT WATER REACTOR SAFETY

SUMMARY

The proposed model of vapor generation following flashing inception consists of heat transfer coefficients for vaporization, vapor-liquid velocity slip and interfacial area density in five flow regimes covering the entire void fraction range. The main formulas are summarized in Table 1.3.

Flashing experiments were conducted with a single beam gamma densitometer system. During these runs, axial pressure distributions were recorded in addition to the transverse chordal averaged void profiles at various axial locations along the test section. For each axial location, an area averaged void fraction was calculated from these transverse void distributions. The present experimental data, in addition to the results presented previously, fulfill the requirements of the proposed test matrix.

Typical results are presented showing the importance of the transverse void profiles. Depending on the profile at the given axial location, differences are observed between the area averaged and the center line (diametral averaged) void fraction values. From these observations, one concludes that in order to make fair comparisons of code calculations which predict area averaged void fractions, with experimental data the point raised above should be carefully considered.

An assessment was completed of how RAMONA-III might be used for analysis of small pipe break LOCAs in LWRs. Our study has given us an understanding of what modifications are necessary to be able to give us this capability. A review of other plant transients was made in order to recommend additions to the plant protection system modelling in RAMONA-III. Work began on implementing the algorithms for calculating reactivity components.

The Mark II once-through steam generator model is being tested in the IRT code. The testing consists of analyzing a transient similar to the Three Mile Island event and comparing the results to a similar analysis using the Mark I modelling.

The RETRAN code has been used to analyze the first of a series of natural circulation tests that are planned to be performed at the Sequoyah PWR plant. These results provide a prediction of the natural circulation capabilities of the reactor during the test.

A loop momentum equation is being incorporated into the IRT code to allow calculation of such cases as natural circulation and pump trip. Results have shown that an implicit integration of the momentum equation is accurate and stable. The inclusion of the pump model into the system equations has been started.

Work on the independent assessment of TRAC-P1A has continued during the reporting period. The assessment with the Moby-Dick nitrogen-water tests has been completed by using the "correct" values for the single-phase liquid

friction factors. This has significantly reduced the sensitivity of TRAC results to the two-phase friction factor options. It has also been found that the slip correlation used in the annular flow regime of the 1-D drift-flux formulation of TRAC-P1A is valid only for the co-current flow. Therefore, the University of Houston flooding tests could not be simulated by using the 1-D components of TRAC.

Simulation of several one-dimensional transient tests, i.e. Super-CANON, Marviken and Battelle-Frankfurt top blowdown tests, has been completed. The flashing delay correlation of Alamgir and Lienhard has been incorporated in the BNL version of TRAC-P1A. Inclusion of this correlation produced the initial pressure undershoot; however, the long-term TRAC-P1A predictions did not change significantly.

Continued efforts on the simulation of RPI phase separation tests and the FRIGG loop tests did indicate some problem areas in TRAC-P1A. These need further investigation. Finally, some improvements in the TRAC plotting package have been accomplished at BNL and sample calculations on the frictional pressure drop in a PWR hot leg during a small break LOCA have been performed.

1. Nonequilibrium Phase Change Studies

1.1 Analytical Modeling (B.J.C. Wu)

It has been shown previously (Wu et al. 1979, Abuaf et al. 1980, Vol II) that the heat transfer limited vapor generation rate following flashing inception is

$$\Gamma_v = A_s \dot{q}'' / L, \tag{1.1}$$

where A_s is the total area of the liquid-vapor interface per unit volume of the mixture, $\dot{q}''$ is the heat flux to the interface and L the latent heat of vaporization. Both A_s and $\dot{q}''$ are flow regime-dependent, and in each flow regime, they are functions of the thermodynamic state and flow variables. Therefore, to calculate A_s and $\dot{q}''$ it is necessary to know, a priori, in which flow regime the system is expected. In this model, the flow regime will be assumed to be a function of the local void fraction α alone. Thus, bubbly flow, bubbly-slug flow, a transitional flow comprising the annular and annular-mist regimes, and finally fully dispersed droplet flow are assumed to occur at successively higher void fraction ranges as shown in Figure 1.1. The void fractions at the transition points are assumed to be

$$\alpha_{b\,max} = 0.3$$

$$\alpha_{s\,max} = 0.8$$

$$\alpha_d = 0.95$$

These values may be modified according to comparison with experiments.

Previously, for $\alpha < 0.3$ the flow was assumed to be in the bubbly regime. A_s was given by

$$A_s = (36 \pi \alpha^2 N_b)^{1/3} = 3\ \alpha / R_b \tag{1.2}$$

where N_b was the number of bubbles per unit volume of the mixture, and R_b was the radius of the bubbles which were supposed to be spherical and of equal size. For $\dot{q}''$, the conduction-dominated model of Plesset and Zwick (1954) or Forster and Zuber (1954) was used. In terms of a heat transfer coefficient

$$h \equiv \dot{q}'' / (T_\ell - T_s) \tag{1.3}$$

$$h = h_{PZ} = \sqrt{3\, k_\ell\, \rho_\ell\, C_p / \pi t} \tag{1.4}$$

where t is the "age" of the bubble, and k_ℓ, ρ_ℓ and $C_{p\ell}$ are the thermal conductivity, density and specific heat of the liquid and T_ℓ and T_s are the liquid and saturation temperatures, respectively. Thus, the earlier model for Γ_v is restricted to low void fractions with a relatively high N_b such that the bubbles are still small even at the upper limit $\alpha = 0.3$ of void fraction.

Then the bubbles remain spherical because of the dominance of surface tension effects; the relative velocity of the bubbles with respect to the liquid remains small such that the convective heat transfer is negligible compared with that due to conduction. To extend the vapor generation model to higher void fractions, these restrictions must be modified.

In the following, the interfacial area densities and the heat transfer coefficients applicable to interfacial heat transfer at each void fraction range shown in Figure 1.1 will be presented.

Void Fraction Range 1. $\alpha = \alpha_o$.

This is the point of flashing inception, and serves as the starting point of vapor generation calculations. The location of flashing inception is to be determined from the flashing inception correlation as discussed in Abuaf et al. (1980) Sec. 6.2. At the inception point, the vapor is assumed to be in the form of critical sized bubbles, with radius R_{cr}:

$$R_{cr} = 2\sigma / (p_s(T_\ell) - p) \quad . \tag{1.5}$$

The critical radius is of the order of a few microns for typical liquid superheat (or pressure undershoot) values found experimentally at flashing inception. At these sizes the bubbles can certainly be considered spherical and move with the liquid with no slip. Thus the model previously used is applicable*:

$$\alpha_o = \frac{4\pi}{3} R_{cr}^3 N_b = 0.0397 (C_p R_{cr})^3, \tag{1.6}$$

$$A_s = 3\alpha_o / R_{cr}, \tag{1.7}$$

and

$$h = h_{pz}. \tag{1.8}$$

Bubbly Flow.

For $\alpha_o < \alpha < \alpha_{b\ max}$, the flow is assumed to be in the bubbly regime. The vapor exists in the form of bubbles of uniform size, although not necessarily spherical. The relative velocity of the bubbles with respect to the liquid $V_{g\ell}$ and the drift velocity V_{gj} are given by (Wallis 1969)

$$V_{g\ell} = v_\infty (1-\alpha)^{n-1} \tag{1.9}$$

$$V_{gj} = v_\infty (1-\alpha)^n \tag{1.10}$$

where n and v_∞ which are respectively an empirical index and the bubble free rise velocity in an infinite liquid, are given in Table 1.1 for the various bubble Reynolds number and size ranges. In region 1 in Table 1.1 the bubbles retain spherical shape and the rise speed is based on the Stokes formula. In

* The constant 0.0397 in Eq. (6) is based on the Plesset and Zwick's (1954) formula and it is different from the one given in Abuaf et al's (1980) Eq. (6-32) which is based on Forster-Zuber's (1954) formula.

region 5 in the Table the bubbles have spherical cap shapes. In between, the bubble shape changes from spherical to spheriodal to ellipsoidal to spherical cap. The rise speeds of steam bubbles in water at three temperatures calculated from these correlations are compared with single bubble air-water experiments at room temperature in Table 1.2 and Figure 1.2. The equivalent sphere radius ω is defined such that the bubble volume

$$V = 4 \pi \omega^3 / 3 \tag{1.11}$$

The discrepancy at large radii (Region 5 in Table 1.1) may be attributed to interference of neighboring bubbles. (Zuber and Hench 1962 as quoted by Wallis 1969). We note, however, that our application of the v_∞ formulas will be limited mostly to ω below the order of 1 cm, above which transition to slug flow occurs.

The steady state heat transfer rate to a spherical bubble moving at constant speed in an infinite liquid is given by the Boussinesque solution (Chao, 1969) which may be expressed as

$$Nu_{\ell,\ ss} = h_{ss} \cdot 2\omega / k_\ell = 2 \sqrt{Pe_\ell / \pi} \tag{1.12}$$

where the subscript ss stands for steady state bubble motion. For spherical caps, the heat transfer rate based on the surface area of the equivalent sphere, is estimated (Davenport, Richardson and Bradshaw 1967) to be about 20% higher than spheres. This estimate agrees with Calderbank and Lochiel's (1964) model, and it is in fair agreement with experiments (Calderbank and Lochiel). Thus, in terms of the heat transf : coefficient based on the equivalent sphere we have

$$h_{ss} = \sqrt{\frac{C_1}{\pi}} \sqrt{\frac{k_\ell \rho_\ell C_{p\ell} V_{g\ell}}{\omega}} \tag{1.13}$$

where $C_1 = 2.0$ for spheres

and $C_1 = 2.88$ for spherical caps.

In our model, we shall assume the transition in bubble shape to occur entirely in Regions 3 and 4 in Table 1.2. Thus we assume that C_1 varies linearly with ω

from $C_1 = 2.0$ at $\omega = 2.21 (\nu_\ell^2 / g)^{1/3} G_1^{-0.0939}$ (1.14a)

to $C_1 = 2.88$ at $\omega = 2 \sqrt{\sigma_\ell / g \rho_\ell}$ (1.14b)

The heat transfer rate to bubbles in transient motion has been studied theoretically by a number of investigators and the resulting expressions are quite complex. In view of the uncertainties associated with the interfacial area, etc. the overall accuracy in Γ_v to be gained by the inclusion of

transient motion effects on bubble growth does not seem to be significant. Thus, for simplicity, the stationary heat transfer coefficient, Eq. (1.4) will be combined with the steady state coefficient to provide a smooth transition, while retaining the correct limit behavior at $t \to 0$ and $t \to \infty$. In the literature, two such combinations have been found:

$$h = \sqrt{h_{p\,Z}^2 + h_{ss}^2} \qquad \text{(Aleksandrov et al. 1967)} \qquad (1.15a)$$

and

$$h = h_{p\,Z} + h_{ss} \qquad \text{(Wolfert 1976)} \qquad (1.15b)$$

Both expressions were based on intuitive physical arguments, and it is not clear which one is more realistic. Both expressions should therefore be compared with experimental data and hopefully one will emerge as the better choice. We note however, that Wolfert's expression will always yield a greater h. It can be shown Eqs. (1.15a and b) are equivalent to

$$h = h_{pZ}\left(1 + \frac{C_1\,\xi}{3}\right)^{1/2}, \qquad \text{(Aleksandrov)} \qquad (1.16a)$$

$$h = h_{pZ}\left(1 + \sqrt{\frac{C_1\,\xi}{3}}\right), \qquad \text{(Wolfert)} \qquad (1.16b)$$

where $\xi = V_{g\ell} \cdot t/\omega$.

Since the h's are defined in terms of the equivalent sphere, the interfacial area density may be calculated from

$$A_{s,b} = 3\,\alpha/\omega, \qquad (1.17)$$

regardless of whether the bubbles are spheres or spherical caps.

In the bubbly flow regime, it is assumed that bubble coalescence does not occur. Thus, the bubble radius changes only as a result of vaporization or condensation at the interface,

$$\frac{d\omega}{dt} = \frac{\dot{q}''}{L\,\rho_g} \qquad (1.18)$$

This equation is equivalent to Eq.(1.1) written on a per unit interfacial area, rather than per unit volume, basis.

Bubbly-Slug Flow.

As the void fraction increases, bubble coalescence becomes more significant. Although in an idealized situation of static, simple cubic configuration of uniform-sized spherical bubbles, geometric interference of bubbles occurs

only when $\alpha > 0.524$,* in reality (Dukler and Taitel 1977) bubble coalescence sets in well below this void fraction value. We shall assume that when $\alpha = \alpha_{b\ max} = 0.3$ some of the bubbles begin to coagulate to form larger bubbles, while the others continue to grow by vaporization according to the rate and mechanism discussed in the last section. Thus, two classes of bubbles coexist in this void fraction range, the larger bubbles formed by coagulation and the smaller, original bubbles. As a result of vaporization at the interface, both classes of bubbles grow, although at different rates. In the meantime, the number of bubbles which have coagulated increases and the population of the smaller class of bubbles thereby decreases. The larger bubbles resulting from coagulation will probably not be spherical. They may either approach the spherical cap shape, or, if ω is comparable or greater than the pipe diameter, acquire an elongated cylinder shape with a rounded head. The latter, bullet shaped bubbles are sometimes called Taylor bubbles, and they are usually separated by liquid (or bubbly liquid) regions, i.e., slugs.

Since vapor generation may take place on the surface of the Taylor bubbles as well as on the small bubbles, the vapor generation rate or the total heat transfer rate is the sum of the two components:

$$\dot{q}''\ A_s = \dot{q}''_T\ A_{s,T} + \dot{q}''_b\ A_{s,b}, \tag{1.19a}$$

or

$$h\ A_s = h_T\ A_{s,T} + h_b\ A_{s,b}, \tag{1.19b}$$

where the subscripts T and b designate quantities pertaining to the Taylor bubbles and the small bubbles respectively. The total interfacial area density is, of course

$$A_s = A_{s,b} + A_{s,T}. \tag{1.20}$$

To estimate the interfacial area density, a few assumptions concerning the partition of the voids between the small bubbles and Taylor bubbles will be made. Referring to the nomenclature for bubbly-slug flow in a circular pipe shown in Figure 1.3, we have the Taylor bubbles, the unit cell, in which one Taylor bubble may be found on the average, and the small bubbles in the bubbly mixture surrounding the Taylor bubbles. We assume that the Taylor bubbles are cylinders of length $2\lambda_T \cdot R_T$ and radius R_T. Thus, their equivalent sphere radius is

$$\begin{aligned} \frac{4\pi\omega_T^3}{3} &= V_T = 2\lambda_T \pi R_T^3 \quad , \\ \omega_T &= (3\lambda_T / 2)^{1/3} R_T \quad , \end{aligned} \tag{1.21}$$

and the surface to volume ratio of the cylinders is

* We point out that this limit is not a function of bubble number density. For a given N_b, the maximum diameter of spheres which may be fitted in a simple cubic lattice is $N_b^{-1/3}$, which corresponds to $\alpha = 0.524$.

$$\frac{S_T}{V_T} = \frac{2\left(\frac{1}{2\lambda_T} + 1\right)}{R_T} = \frac{2\left(\frac{1}{2\lambda_T} + 1\right)}{\omega_T \left(\frac{2}{3\lambda_T}\right)^{1/3}} \quad . \tag{1.22}$$

For comparison, the surface to volume ratio of spherical caps (subscript c) is

$$\frac{S_c}{V_c} = \frac{3\ (3-2\xi-\xi^2)}{R_c\ (2-3\xi+\xi^3)} = \frac{3\ (3-2\xi-\xi^2)}{\omega_c \left[2\ (2-3\xi+\xi^3)\right]^{2/3}} \quad , \tag{1.23}$$

where $\xi = \cos\ \phi$ of the spherical caps, ϕ being the half substended angle, and R_c is the radius of the cap. The quantity $(S/V)\cdot\omega$ for cylinders and spherical caps are plotted as functions of λ and ξ respectively, in Figure 1.4. For most spherical cap bubbles, $\phi \approx 50°$ or $\xi \approx 0.6$ and their surface to volume ratio is not too different from cylinders with λ's of 4 or 5. Thus, we shall assume all large bubbles formed by coalescence of small bubbles to be of cylindrical shape, with λ to be optimized in comparison with experiments.

Next, we shall assume that $\lambda_c = \lambda_T = \lambda$, i.e., the unit cell is geometrically similar to the Taylor bubble and we shall drop the subscript on from now on. Thus, the void fraction of the Taylor bubbles is

$$\begin{aligned} \alpha_T &= \frac{V_T}{V_c} = \frac{8\ R_T^3}{D^3} \\ &= \frac{16}{3\lambda} \left(\frac{\omega_T}{D}\right)^3 \quad , \end{aligned} \tag{1.24}$$

where V_c is the volume of the unit cell and the number density of the Taylor bubbles is

$$N_T = \frac{1}{V_c} = \frac{4}{\pi\ \lambda\ D^3} \quad , \tag{1.25}$$

and the interfacial area density of the Taylor bubbles is

$$A_{s,T} = \frac{S_T}{V_T} \cdot \alpha_T = 4\left(\frac{1}{2\lambda} + 1\right) \frac{\alpha_T^{2/3}}{D} \quad . \tag{1.26}$$

For a given pipe diameter, $A_{s,T}$ can be found as a function of α_T for prescribed values of λ.

The average void fraction of the bubbly-slug flow should include vapor volumes in the Taylor bubbles as well as the small bubbles. Denoting the volume of a small bubble by V_b, we have

$$\alpha = \frac{V_T + \Sigma V_b}{V_c} = \alpha_T + \alpha_b \tag{1.27}$$

where $\alpha_b = \Sigma V_b / V_c$ is the void fraction of the small bubbles. In addition, we define α_b' as the void fraction of the small bubbles based on the volume of the bubbly mixture, i.e.,

$$\alpha_b' = \Sigma V_b / (V_c - V_T). \tag{1.28}$$

hence

$$\alpha_b = \alpha_b' (1 - \alpha_T) \tag{1.29}$$

and from Eq. (1.27),

$$\alpha_T = (\alpha - \alpha_b') / (1 - \alpha_b'). \tag{1.30}$$

Combination of Eqs. (1.30) and (1.26) yields $A_{s,T}$ as a function of α, with α_b', λ and D as parameters. For $A_{s,b}$ in bubbly-slug flow, we use the expression for the equivalent spheres (see Eq. 1.17)

$$A_{s,b} = \frac{3}{a_b} \alpha_b . \tag{1.31}$$

It finally remains to specify α_b'. Consistent with our earlier assumption that bubble coalescence starts at $\alpha = \alpha_{b\ max}$, we suppose that the local void fraction in the bubbly region of bubbly-slug flow should never exceed $\alpha_{b\ max}$. Thus, as the average void fraction α increases beyond $\alpha_{b\ max}$, some small bubbles are removed from the bubbly region to form Taylor bubbles, and α_b' is bounded by $\alpha_{b\ max}$, i.e.,

$$\alpha_b' = \alpha_{b\ max} . \tag{1.32}$$

With this assumption, we visualize the following sequence of events. First a fixed population of bubbles was formed as a result of nucleation, with the initial radius R_{cr} and concentration N_b as given by Eq. (1.6). The entire population of bubbles then grew according to the rate Eq. (1.18). At this stage (the bubbly flow range) the bubble population remained fixed, since no further nucleation was assumed (Wu et al. 1979), and no bubble coalescence or disintegration occurred*. As the bubbles continued to grow and their (equivalent) radius became greater than the value corresponding to $\alpha = \alpha_{b\ max}$ coagulation was attained to "relieve the congestion" of the bubbles by forming relatively isolated large (Taylor) bubbles. The bubble population was reduced and the local bubble concentration in the bubbly portion adjusted itself such that the local void fraction α_b' remained constant at $\alpha_{b\ max}$. In other words, the "excess" void fraction was accommodated in the Taylor bubbles. This situation is depicted in Figure 1.5.

It is recognized that for α not too much greater than $\alpha_{b\ max}$, the larger

* Although N_b would change because the system volume would increase with α.

bubbles formed by coagulation are not likely to have the elongated shape of Taylor bubbles and will probably be spherical caps. However, we shall ignore the small difference in the A_s for spherical caps and cylinders in this treatment.

The heat transfer rate to the small and Taylor bubbles are both needed for the total vapor generation rate calculation. The heat transfer coefficient h_b to the small bubbles will be assumed to be the same as those for the bubbly flow, Eqs. (1.16a and b), except for one modification of the slip velocity to reflect the presence of the Taylor bubbles. We shall return to this shortly.

We were unable to find a heat transfer coefficient to Taylor bubbles. However, since the majority of the interface on the Taylor bubble is the lateral surface of the cylinder, this area is probably responsible for the majority of the heat transfer as well. The heat transfer coefficient to the cylindrical surfaces will be approximated by that for the liquid films. This approximation is the same as that in the TRAC model for slug flows. (TRAC-P1A manual and Rohatgi and Saha 1979). Linehan (1968) has measured the heat transfer coefficient over subcooled liquid films during condensing heat transfer of steam and obtained at the correlation:

$$St_\ell = \frac{Nu_\ell}{Re_\ell \; Pr_\ell} = \text{const} = 0.0073, \tag{1.33}$$

i.e., $$h_T = 0.0073 \; \rho_\ell \; V_{g\ell} \; c_{p\ell}. \tag{1.34}$$

We note that in the TRAC model the Prandtl number dependence has been neglected in Eq. (1.33) and h_T becomes $h_T = 0.0073 \; \rho_\ell \; k_\ell \; V_{g\ell} / \mu_\ell$.

This assumption obviously has limited validity. The search for a heat transfer correlation for Taylor bubbles should continue and improvement to Eq. (1.34) should be made.

The drift and slip velocities in slug flow have been given by Zuber and Findley (1965):

$$V_{gj,T} = 0.35 \sqrt{\frac{g \; (\rho_\ell - \rho_g) \; D}{\rho_\ell}}, \tag{1.35}$$

$$V_{g\ell,T} = V_{gj,T} \; / \; (1 - \alpha) \; . \tag{1.36}$$

However, in the low α range of the bubbly-slug regime, the flow field is still dominated by the small bubbles, not the small number of Taylor bubbles. So the slip velocity should still be influenced mostly by the rise speeds of the small bubbles, no discontinuous change in $V_{g\ell}$ and V_{gj} from those given in Table 1.1 to Eqs. (1.35) and (1.36) is to be expected. We assume the slip velocity

in bubbly-slug flow to be given by the average

$$V_{g\ell} = (\alpha_b V_{g\ell,b} + {}_T V_{g\ell,T}) / \alpha \quad (1.37)$$

and

$$V_{gj} = (1 - \alpha) V_{g\ell}, \quad (1.38)$$

where $V_{g\ell,b}$ is to be determined from formulas in Table 1.1 and $V_{g\ell,T}$ from Eq. (1.36). The slip velocity calculated from Eq. (1.37) is to be used in the calculation of the heat transfer coefficients h_b and h_T in the bubbly-slug regime.

To summarize, it is assumed that for $\alpha_{b\ max} < \alpha < \alpha_{s\ max}$, bubbly-slug flow prevails, where $\alpha_{s\ max}$ is the maximum void fraction for which slug flow is important. In the bubbly-slug regime voids exist in either one of two forms, namely, small bubbles and Taylor bubbles (Eq. 1.27). The void fraction is partitioned between the two according to Eqs. (1.29) and (1.30) with α_b' fixed at $\alpha_{b\ max}$ (Eq. 1.32). The interfacial area densities of the two forms of voids are expressed in terms of the void fraction, the length to diameter ratio of the Taylor bubbles, the pipe diameter, and the equivalent radius of the small bubbles (Eqs. 1.26 and 1.31). The heat transfer coefficients are Eq. (1.34) for Taylor bubbles and those in Eq. (1.16a and b) for the small bubbles with the bubble growth rate given by Eq. (1.18). For the slip velocity Eq. (1.37) will be adapted. Total heat transfer rate is to be calculated from Eq. (1.19). The upper limit of bubbly-slug flow may be assumed to be $\alpha_{s,max} = 0.8$.

Transition Regime and Annular Mist Flow.

Behavior in this regime is not well understood. A model for liquid entrainment is needed to estimate the fraction of liquid which is in the dispersed droplet form, the balance being assumed to be in a film on the pipe wall. The entrainment models found in the literature, namely Wallis (1968), and Paleev and Filippovich (1966) do appear to be adequate.

No particular expressions for A_s and h are recommended. The vapor generation rate Γ_v in this regime will be interpolated between the Γ_v calculated for the bubbly-slug regime and the next regime, the fully dispersed droplet flow.

Dispersed Droplet Flow.

When $\alpha > \alpha_d$, the liquid is assumed to be fully dispersed as droplets. The value of α_d is assumed to be 0.95. In the dispersed droplet regime, the droplet size is stabilized by the balance between the surface tension and aerodynamic forces; the droplet diameter may be expressed in terms of a critical droplet Weber number

$$We_d = \frac{\rho_g V_{g\ell}^2 d}{\sigma_\ell} \quad (1.39)$$

Wallis (1969) gave the critical Weber number of 12 for droplets in a low

viscosity carrier gas, whereas Gyarmathy (1976) found the literature value of We_d in the range

$$8 < We_{d\ cr} < 15.$$

It appears Wallis' value of 12 is reasonable, therefore

$$d = \frac{12\ \sigma_\ell}{\rho_g\ V_{g\ell}^2} \quad . \tag{1.40}$$

We note that in the TRAC-P1A manual, a critical Weber number of 5 is quoted. However, according to Rohatgi and Saha (1979) the value used in the TRAC Code is actually 2. This value seems too low compared to the majority of values quoted in the literature. Assuming spherical droplets, we have

$$A_{s,d} = \frac{6\ (1 - \alpha)}{d} \tag{1.41}$$

The slip velocity of droplets is given by Wallis (1969)

$$V_{g\ell} = \frac{1.4}{\alpha} \left[\frac{g\ \sigma_\ell\ (\rho_\ell - \rho_g)}{\rho_g^2} \right]^{1/4} , \tag{1.42}$$

which has a similar form as that of Region 5 in Table 1.1, except that ρ_ℓ is replaced by ρ_g in the denominator. The drift velocity in droplet flow is

$$V_{gj} = \alpha\ V_{g\ell} . \tag{1.43}$$

The convective heat transfer to liquid droplets has been investigated by a number of researchers. Most of the data may be correlated by the expression

$$Nu_d = 2.0 + C_3\ Re_d^{1/2}\ Pr_g^{1/3}, \tag{1.44}$$

where the droplet Nusselt number is

$$Nu_d = h_d\ d/k_g, \tag{1.45}$$

the droplet Reynolds number is

$$Re_d = \frac{\rho_g\ V_{g\ell}\ d}{\mu_g} \tag{1.46}$$

and the vapor Prandtl number is

$$Pr_g = \frac{C_{pg}\ \mu_g}{k_g} \tag{1.47}$$

Ranz and Marshall (1952) found $C_3 = 0.6$ for various liquid or solid spheres in air or other fluids. Lee and Ryley (1968) conducted experiments of evaporation of water droplets in superheated steam and found that $C_3 = 0.74$, for the Reynolds number range of 64 to 250. Comparison of Lee and Ryley's correlation with the data and correlation of Ranz and Marshall is shown in Figure 1.6. It appears that the two agree quite well and that Lee and Ryley's correlation may be valid for droplet Reynolds numbers up to 40000. Therefore Lee and Ryley's (1968) correlation will be used for dispersed droplet flows.

1.2 Flashing Experiments (G.A. Zimmer, N. Abuaf, J.H. Klein and B.J.C. Wu)

After the initiation of the experiments during the first period of this quarterly, the main pump of the loop sheared its shaft and had to be replaced with a spare pump that was obtained from surplus. The silver epoxied electrical connections of the five cadmium Telluride detectors mounted on the printed circuit board deteriorated due to the high temperature and high humidity environment coupled with the strong vibrations of the test section. This deterioration of the connections caused spurious signals to be generated in the preamplifiers. Since we were unable to fix the five beam system within the available time, a decision was made to shift to a single beam system with the detector crystal encased in a hermetically sealed BNC connector. The single beam densitometer, source holder and detector, was mounted on the traversing mechanism allowing transverse void profiles to be obtained at the 27 axial locations along the test section. The test section was recalibrated for both water full and empty (full of air) with the single beam gamma densitometer system and experiments were conducted under various flashing conditions. During all the runs, axial pressure distributions were recorded in addition to the transverse chordal averaged void profiles at various axial locations. These transverse void distributions were used in the calculation of the area averaged void fraction for each axial location. These obtained experimental data coupled to the results presented in our previous quarterlies and reports complete the requirements of the proposed Test Matrix.

All the details of the data will be presented in the final report which is in preparation. However, some typical results will be presented in the following section and Figures.

The first series of experiments presented in Figures 1.7, 1.8, 1.9, 1.10, 1.11 and 1.12, were all performed at 149°C inlet temperature. During these runs the mass flow rate was varied from 5.8 to 13.1 kg/s. This low limit of mass flow rate corresponds to a single phase flow through the whole test section as presented in Figures 1.7a and 1.7b. The pressure drop across the venturi shows the typical single phase pressure recovery in the diverging section, while the area averaged axial void profile, shows that the flow is all single phase in the test section. Results presented in Figure 1.8 conducted at 6.4 kg/s, shows the typical pressure and void profiles obtained with the condensation front sitting in the diverging section of the nozzle. The increase of the mass flow rate to 7.2 kg/s (Figure 1.9) 8.7 kg/s (Figure 1.10), 11.6 kg/s (Figure 1.11) and 13.1 kg/s (Figure 1.12) is accompanied by a leveling of the pressure profile in the diverging section and increase of the local area averaged void fraction.

In Figure 1.11a, the area averaged alpha profiles are compared to the diametral averaged void fraction that would be measured along the centerline of the test section. For this experiment, which was performed at 11.6 kg/s, the two agree quite well with each other. The detailed transverse void distributions for this case are presented in Figure 1.13 for the four axial locations corresponding to pressure tap locations of 47, 45, 43 and 41. The transverse void distributions at every axial locations 1.13a, b, c, d appear to be asymmetrical with respect to the test section centerline, with the highest voids being generated on the left hand side which corresponds to the pressure tap locations.

The same comparison between the area averaged alpha with the centerline alpha is also presented in Figure 1.12 for a mass flow rate of 13.1 kg/s. Here the centerline void fraction is lower than the area averaged value. This fact is clearly observable in Figure 1.14 which represents the transverse void profiles at four axial locations corresponding to pressure taps 47, 45, 43 and 41. In these distributions Figures 1.14a, b, c, and d, the transverse void distribution shows less an asymmetry than the ones presented in Figure 1.13.

Additional experiments were also performed for an inlet temperature of 149°C and 8.7 kg/s mass flow rate, while varying the condensing tank pressure by additional spray cooling. The axial pressure distributions for this test are presented in Figure 1.15b. In Figure 1.15a, the comparison of the area averaged void fraction is made with the corresponding center line diametrial void fraction distribution where the difference between the two is more pronounced. This discrepancy can be explained by observing Figure 1.16 which depicts the detailed transverse void profiles at four axial locations corresponding to taps 47, 45, 43 and 41. This void profile shows a low void core surrounded by a high void region along the walls and is quite symmetrical with respect to the centerline.

As stated above, all the detailed information and data of these results will be presented in the final report in addition to the experiments conducted under other flow conditions.

These results clearly show the importance and effect of the transverse void fraction profiles on the area averaged or center line (diametral averaged) values. Thus, to make fair comparisons between code predictions and experiments these effects must carefully be considered.

REFERENCES

ABUAF, N., WU, B. J. C., ZIMMER, G., and JONES, O. C., (1980) BNL-NUREG-27138.

ALEKSANDROV, Yu. A., VORONOV, G. S., GORBUNKOV, V. M., DELONE, N. B., and NECHAYEV, Yu. I., (1967) Bubble Chambers, Indiana University Press, (Bloomington, Indiana).

CALDERBANK, P. H. and LOCHIEL, A. C., (1964) Chem. Eng. Sci., 19, 485.

CHAO, B. T., (1969) J. Heat Transfer, 91, 273.

DAVENPORT, W. G., RICHARDSON, F. D., and BRADSHAW, A. V., (1967) Chem. Eng. Sci. 22, 1221.

DUKLER, A. E., and TAITEL, Y., (1977) NUREG-0162 (1977) University of Houston.

FORSTER, H. K., and ZUBER, N., (1954) J. Appl. Phys. 25, 474.

GYARMATHY, G., (1976) Two Phase Steam Flow in Turbines and Separators, pp. 49-50, Edited by M. J. Moore and C. H. Sieverding, (McGraw-Hill, N.Y.)

HABERMAN, W. L., and MORTON, R. K., (1956) Trans. Am. Soc. Civ. Eng. 121, 227.

LEE, K., and RYLEY, D. J., (1968) J. Heat Transfer 90, 445.

LINEHAN, J. H., (1968) ANL-7444.

PALEEV, I. I., and FILIPPOVICH, B. S., (1966) Int. J. Heat Mass Transfer 9, 1089.

PLESSET, M. S., and ZWICK, S. A., (1954) J. Appl. Phys. 25, 493.

RANZ, W. E., and MARSHALL, W. R., (1952) Chem. Eng. Prog. 48, 141-146 and 173-180.

ROHATGI, U. S., and SAHA, P., (1979) Constitutive Relations in TRAC-P1A, BNL Report to be published.

TRAC-P1A, An Advanced Best-Estimate Computer Program for PWR LOCA Analysis. (LASL).

WALLIS, G. B., (1968) Int. J. Heat Mass Transfer, 11, 783.

WALLIS, G. B., (1969) One-Dimensional Two-Phase Flow (McGraw-Hill, N.Y.).

WOLFERT, K., (1976) The Simulation of Blowdown Processes with Consideration of Thermodynamic Nonequilibrium Phenomena - Paper presented at OECD Specialist's Meeting on Transient Two-Phase Flow, Toronto 1976.

WU, B. J. C., SAHA, P., ABUAF, N., and JONES, O. C., (1979) BNL-NUREG-25709.

ZUBER, N., and FINDLEY, J. A., (1965) J. Heat Transfer 87, 453.

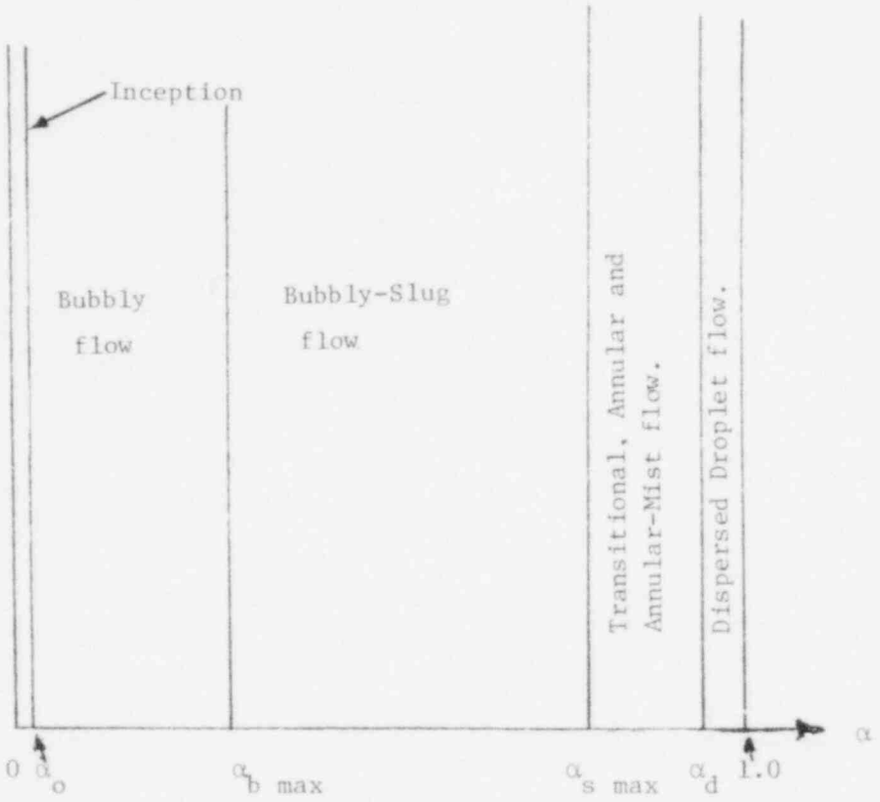

Figure 1.1. Flow Regimes.

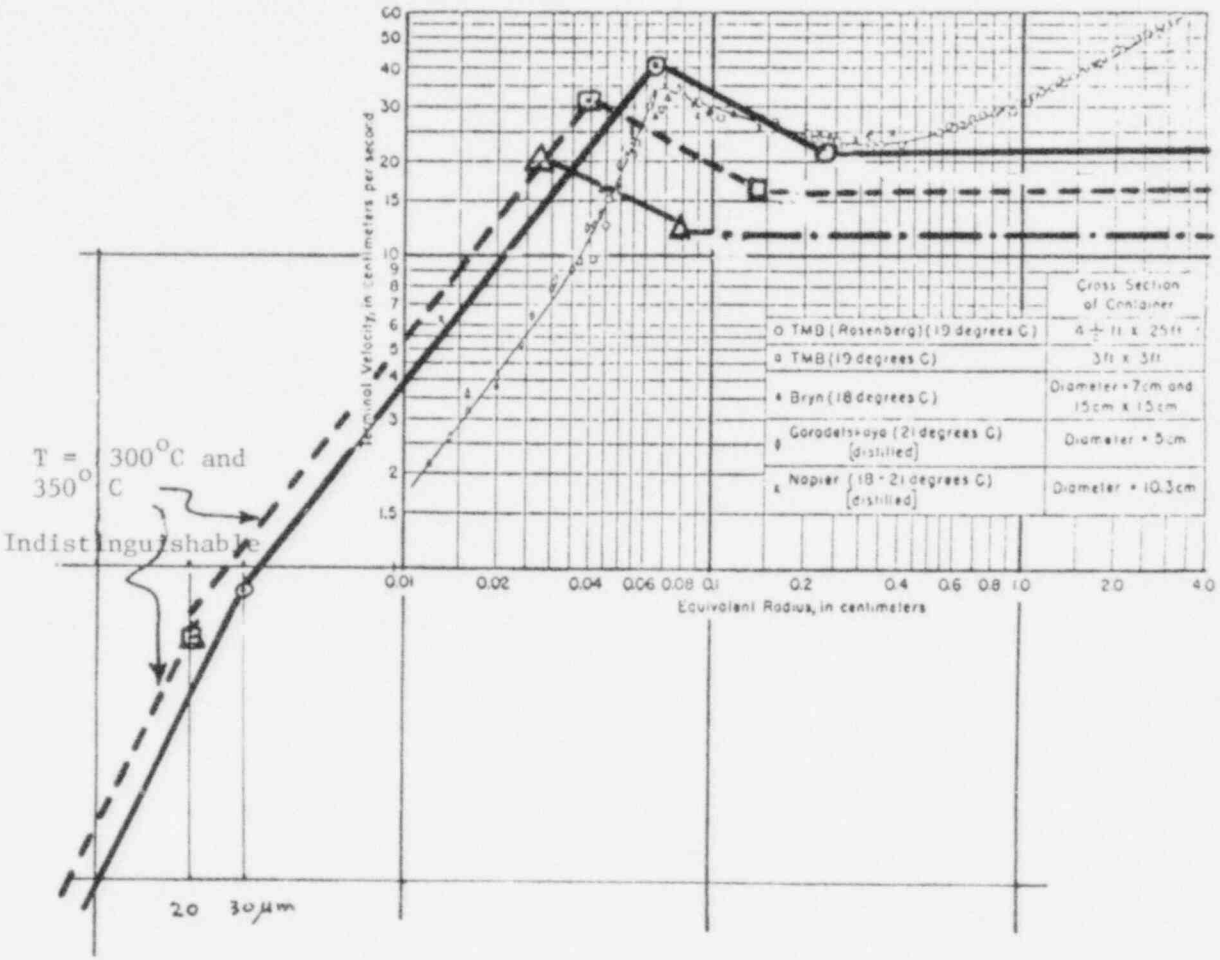

Figure 1.2. Comparison of Correlation of Table I with Experiment.

Calculations: T = 120°C
300°C
350°C
Water - Steam bubbles

Experiments: Air-water from Haberman and Morton (1953)

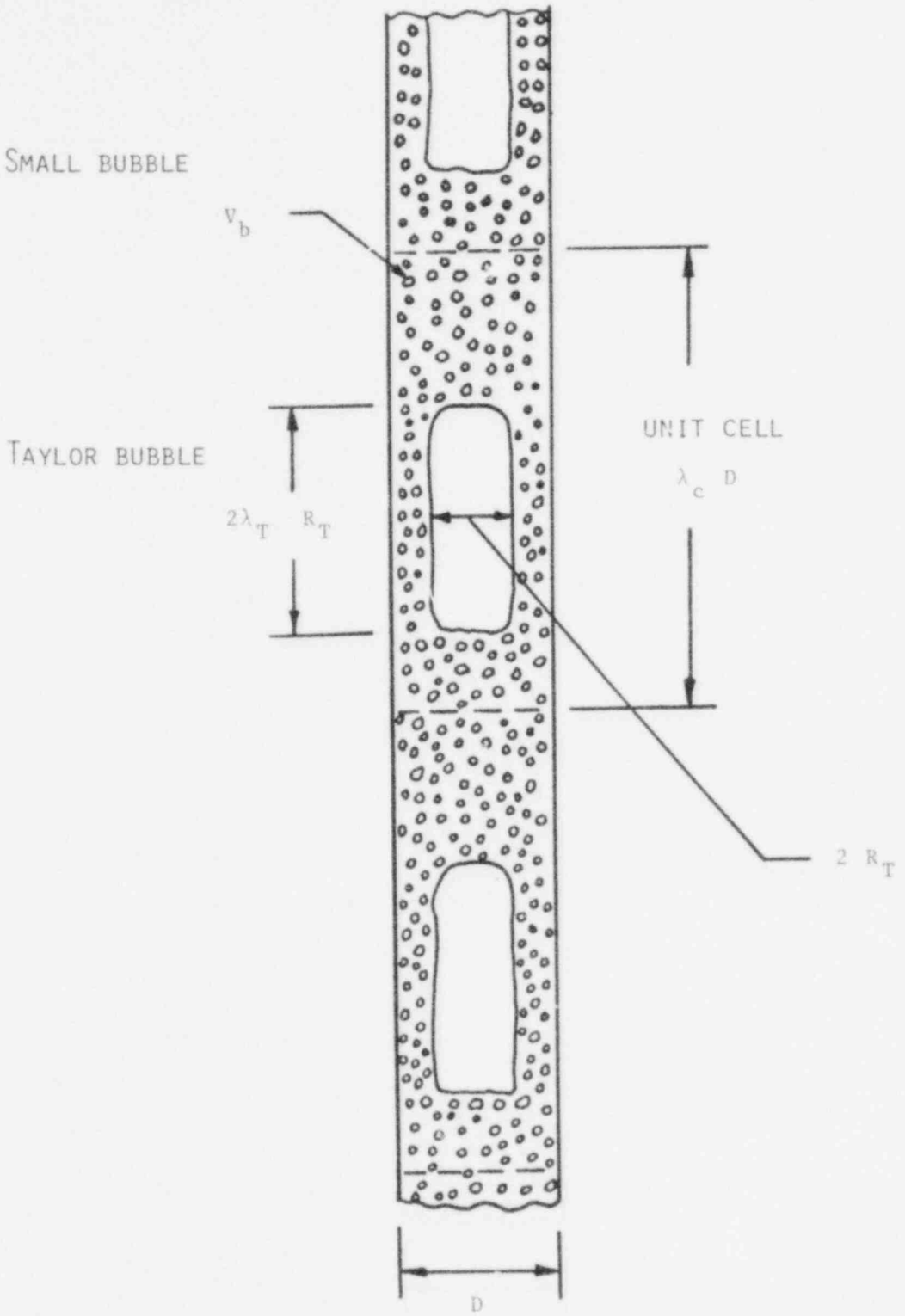

Figure 1.3. Nomenclature of Bubbly-Slug Flow.

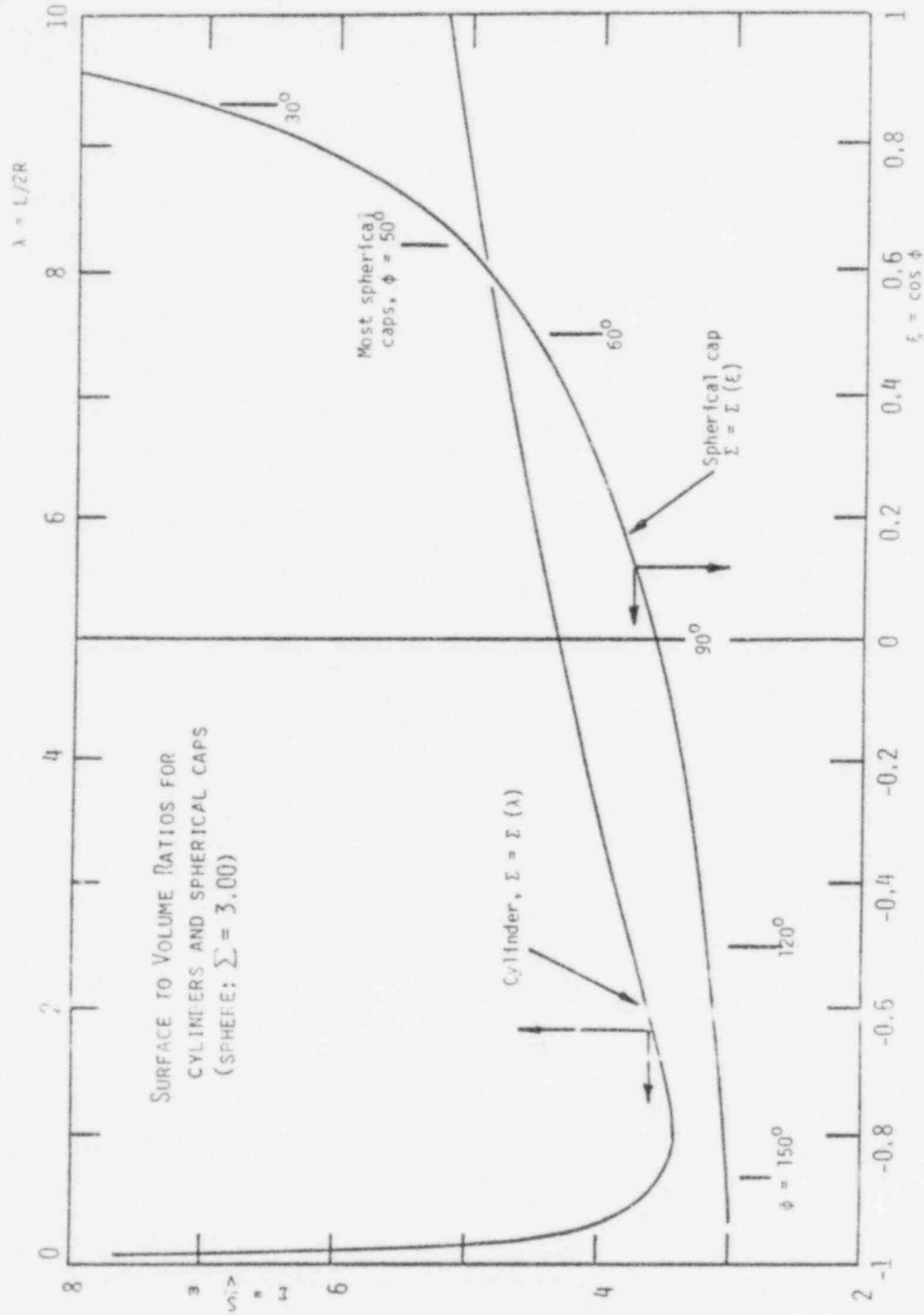

Fig. 1.4 Surface to Volume Ratios.

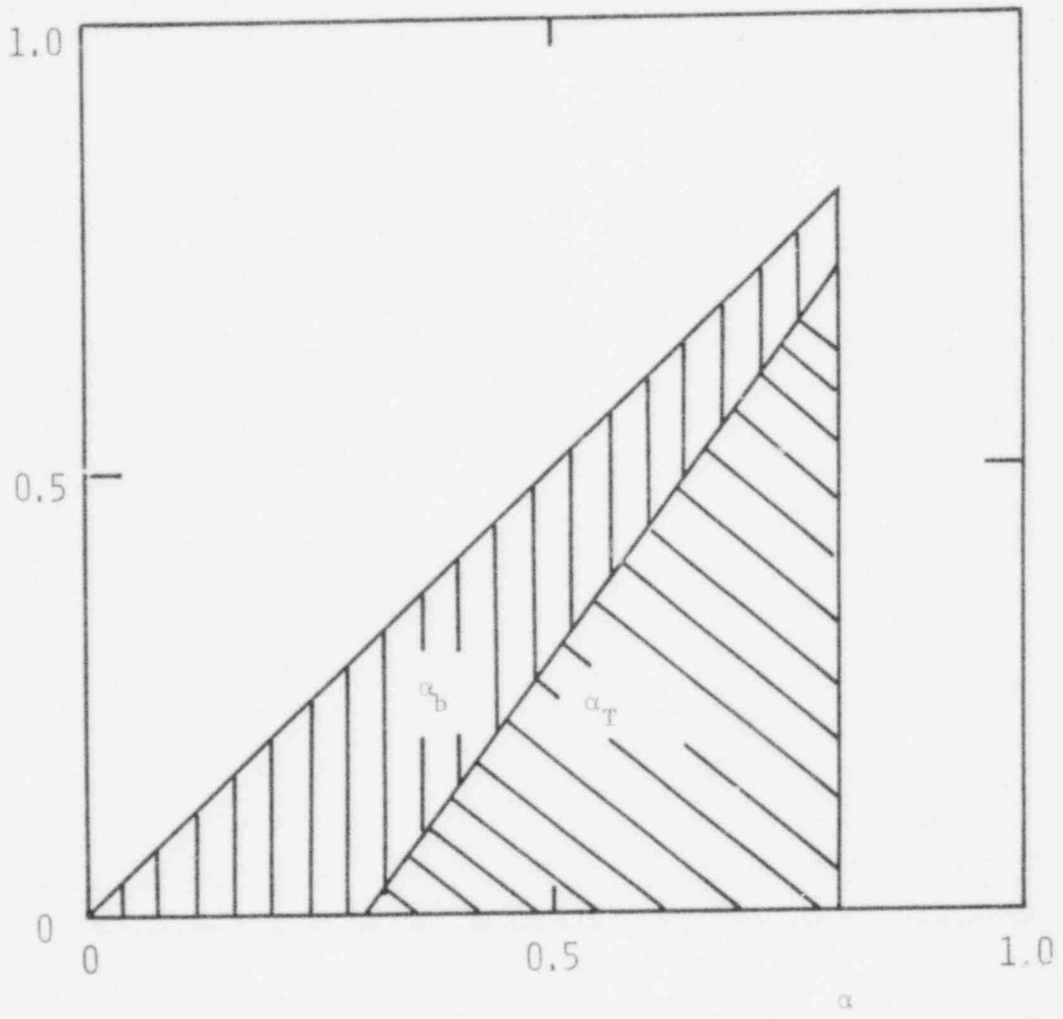

Figure 1.5. Partition of voids in Bubbly and Bubbly-Slug flows, Equations (1.29), (1.30) and (1.32) with $\alpha_{b\ max} = 0.3$, $\alpha_{s\ max} = 0.8$.

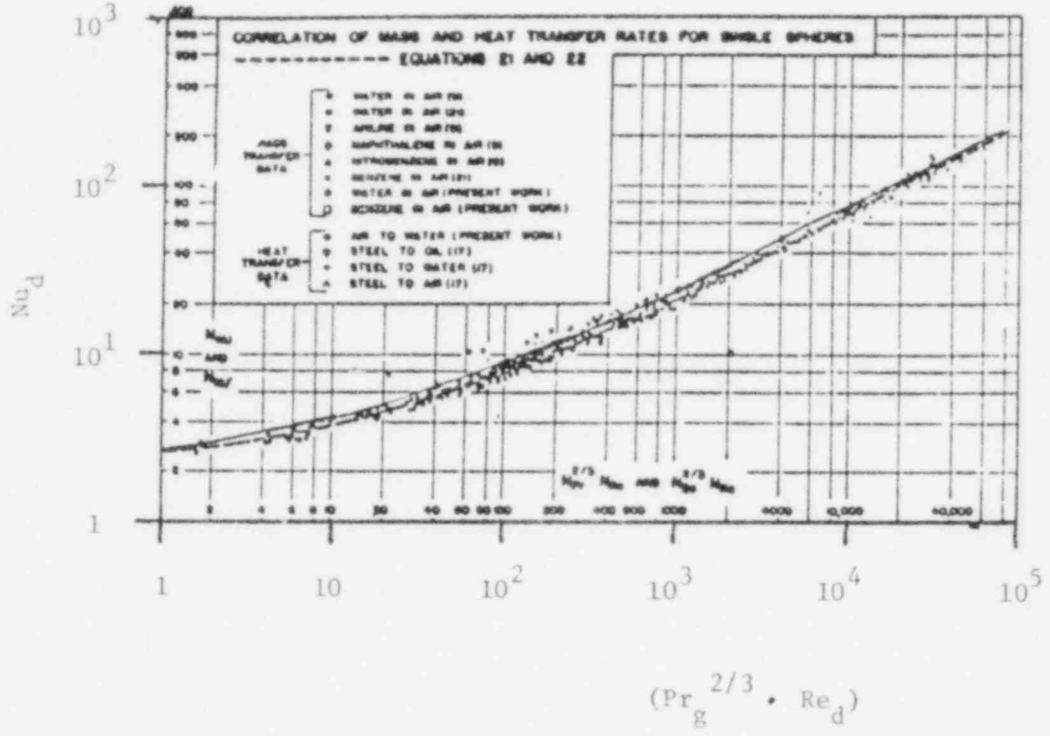

Figure 1.6. Heat and mass transfer rate to spheres. Original data and correlation (--------) from Ranz and Marshall (1952). Correlation of Lee and Ryley (1968) is superimposed (————).

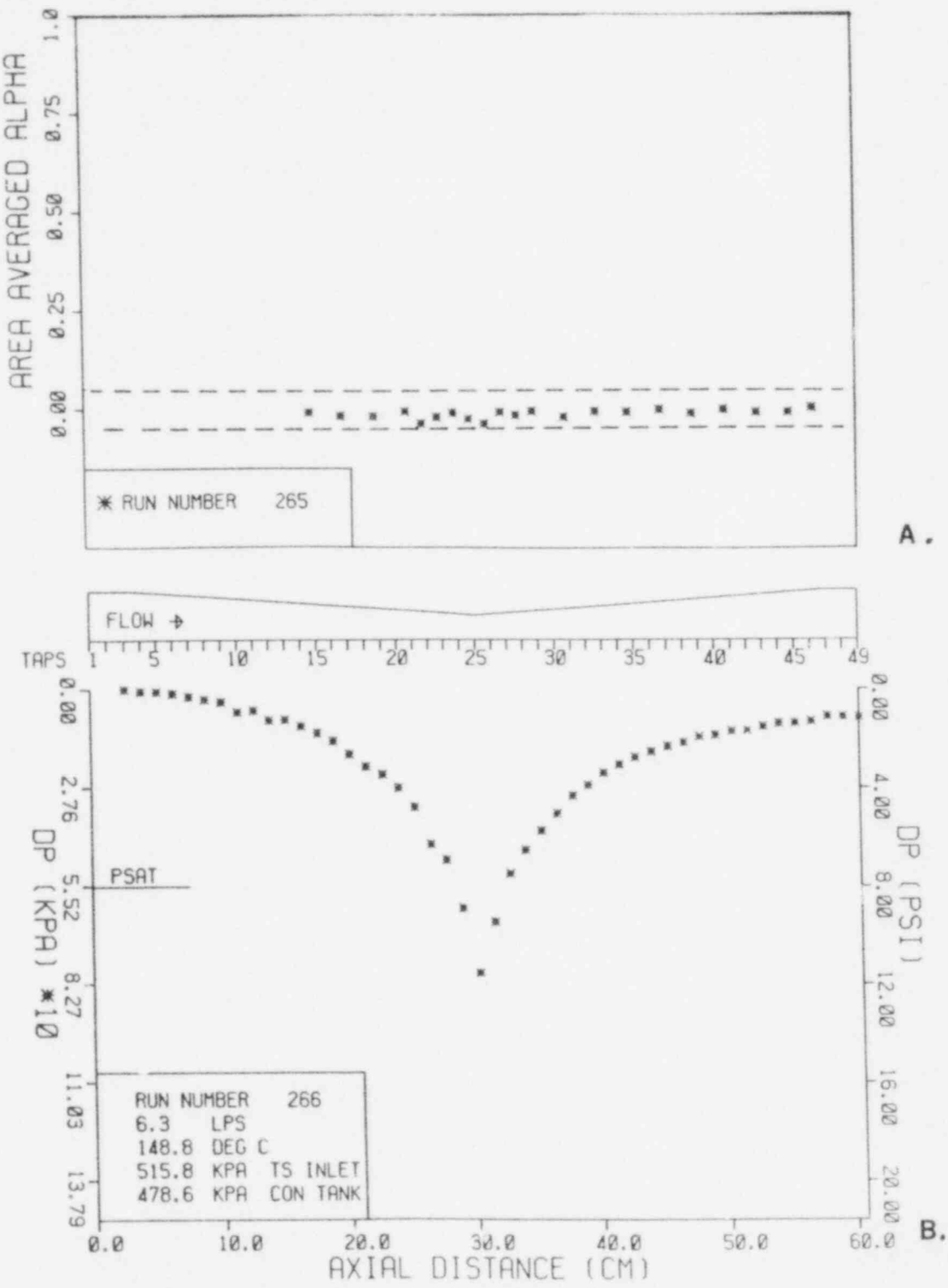

Figure 1.7. Axial distributions of the area-averaged void fraction (A) and of the pressure drop (B) in the test section. Runs 265 and 266 were performed at the following conditions: p_{in}= 515.8 kPa, T_{in}= 148.8 C, p_{ct}= 478.6 kPa and at a mass flow rate of 5.8 kg/s. The broken lines in A represent the $\pm$ 0.05 values for the void fraction. (BNL Neg. No. 6-953-80).

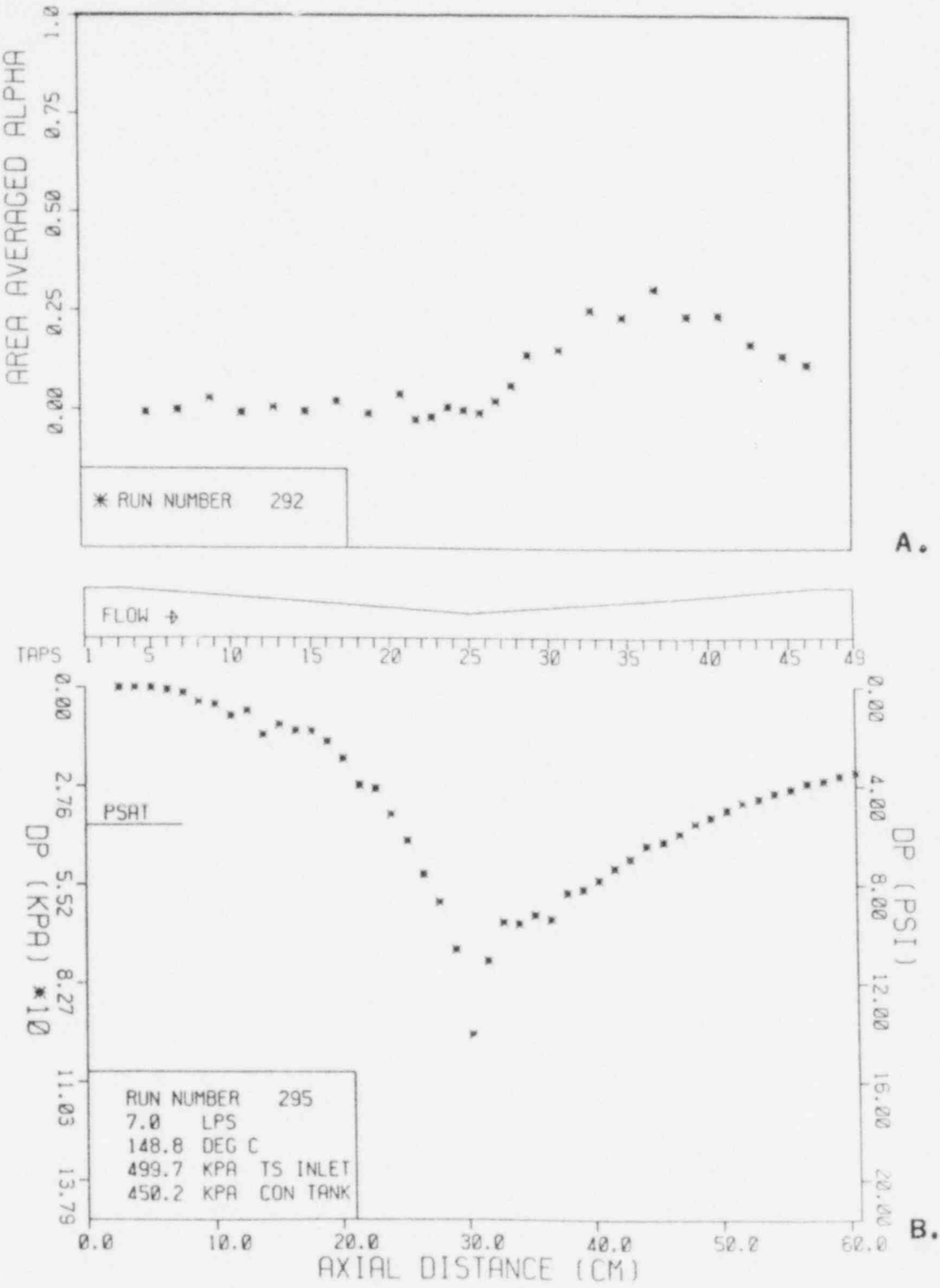

Figure 1.8. Axial distributions of the area averaged-void fraction (A) and of the pressure drop (B) in the test section. Runs 292 and 295 were performed at the following conditions: p_{in}= 499.7 kPa, T_{in}= 148.8 C, p_{ct}= 450.2 and at a mass flow rate of 6.4 kg/s. (BNL Neg. No. 6-951-80).

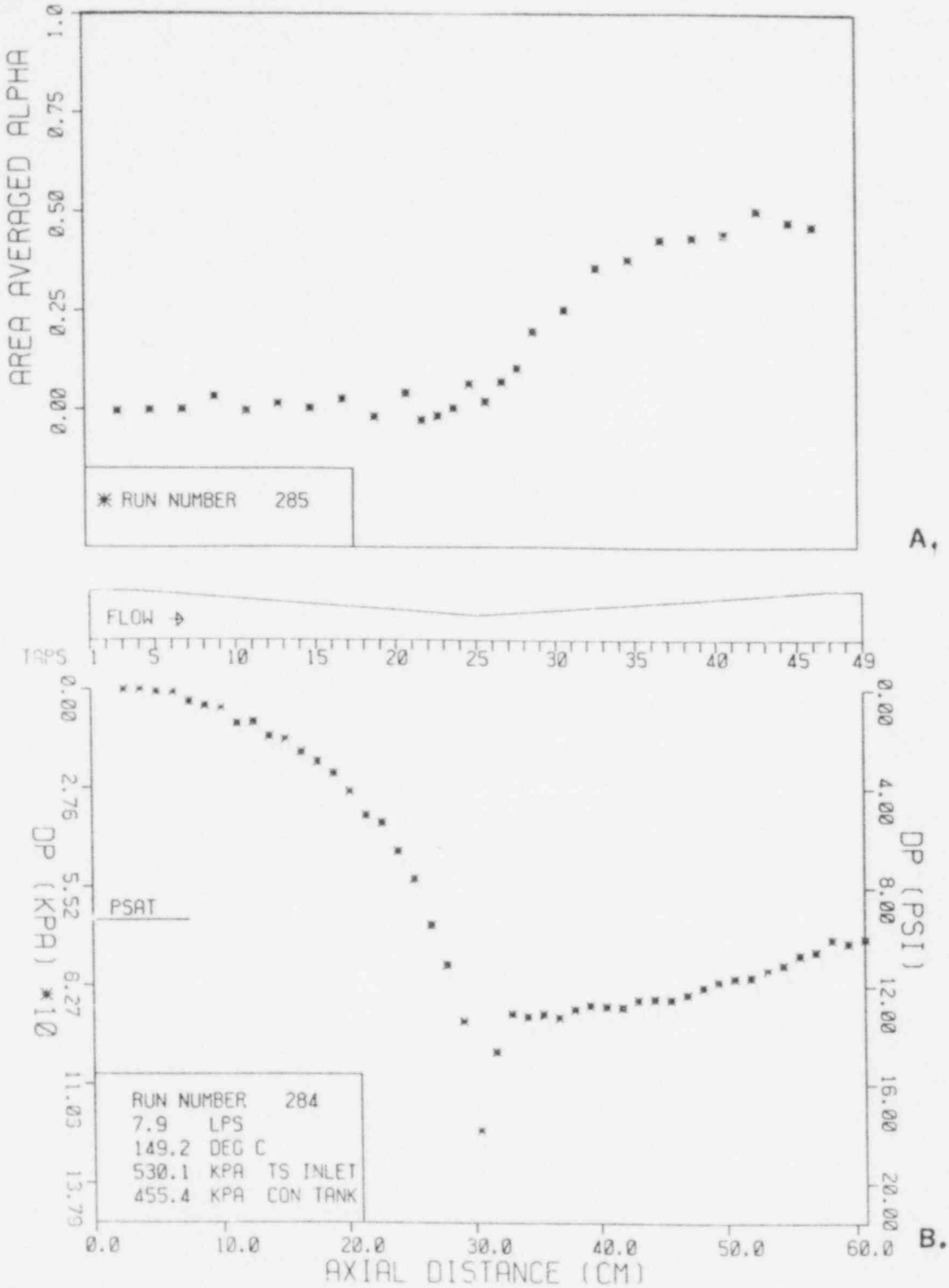

Figure 1.9. Axial distributions of the area averaged-void fraction (A) and of the pressure drop (B) in the test section. Runs 284 and 285 were performed at the following conditions: p_{in}= 530.1 kPa, T_{in}+ 149.2 C, p_{ct}= 455.4 kPa, and at a mass flow rate of 7.9 kg/s. (BNL Neg. No. 6-954-80).

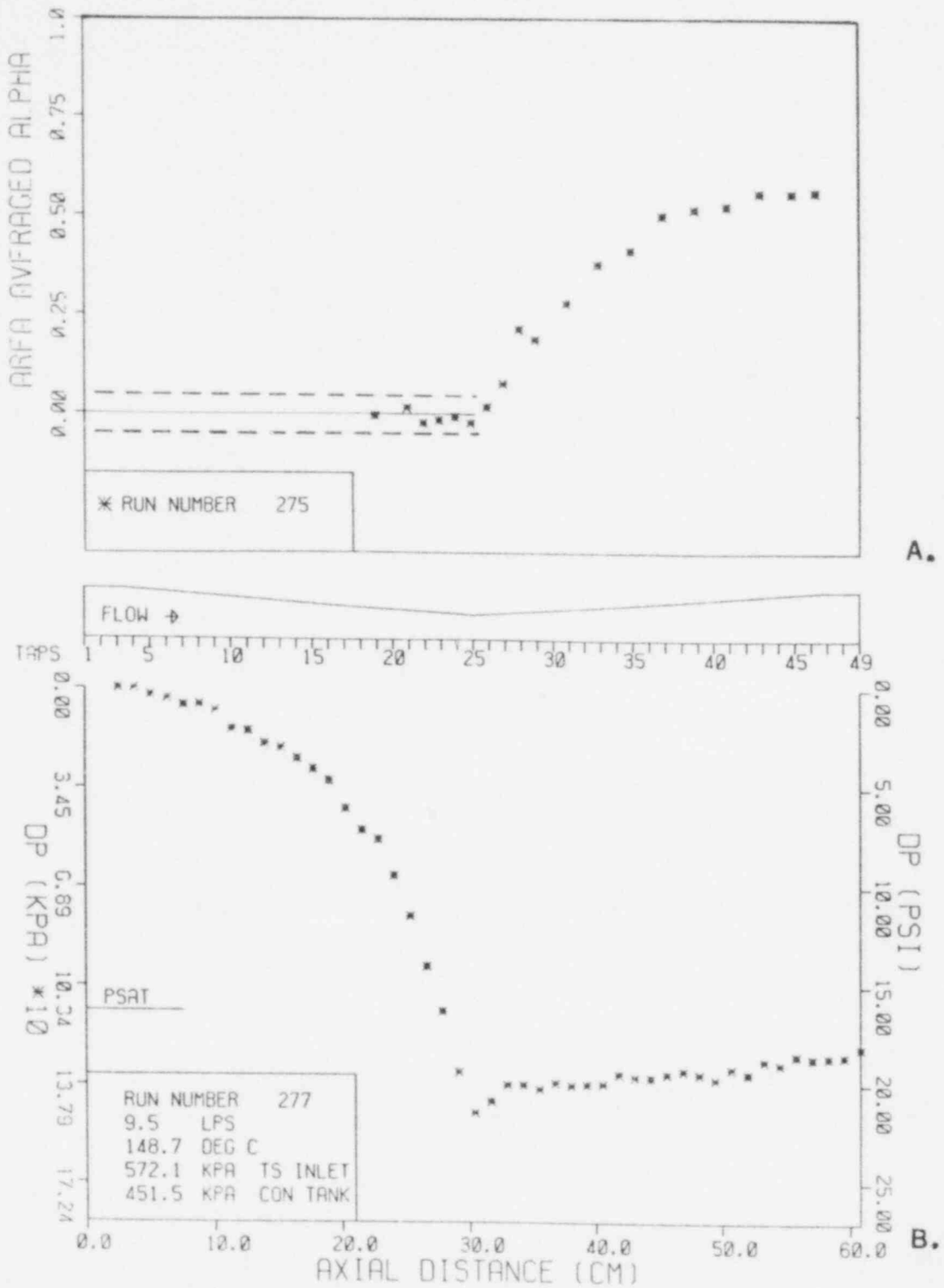

Figure 1.10. Axial distributions of the area-averaged void fraction (A) and of the pressure drop (B) in the test section. Runs 275 and 277 were performed at the following conditions: p_{in}= 572.1 kPa, T_{in}= 148.7 C, p_{ct}= 451.5 kPa and at a mass flow rate of 8.7 kg/s. (BNL Neg. No. 6-952-80).

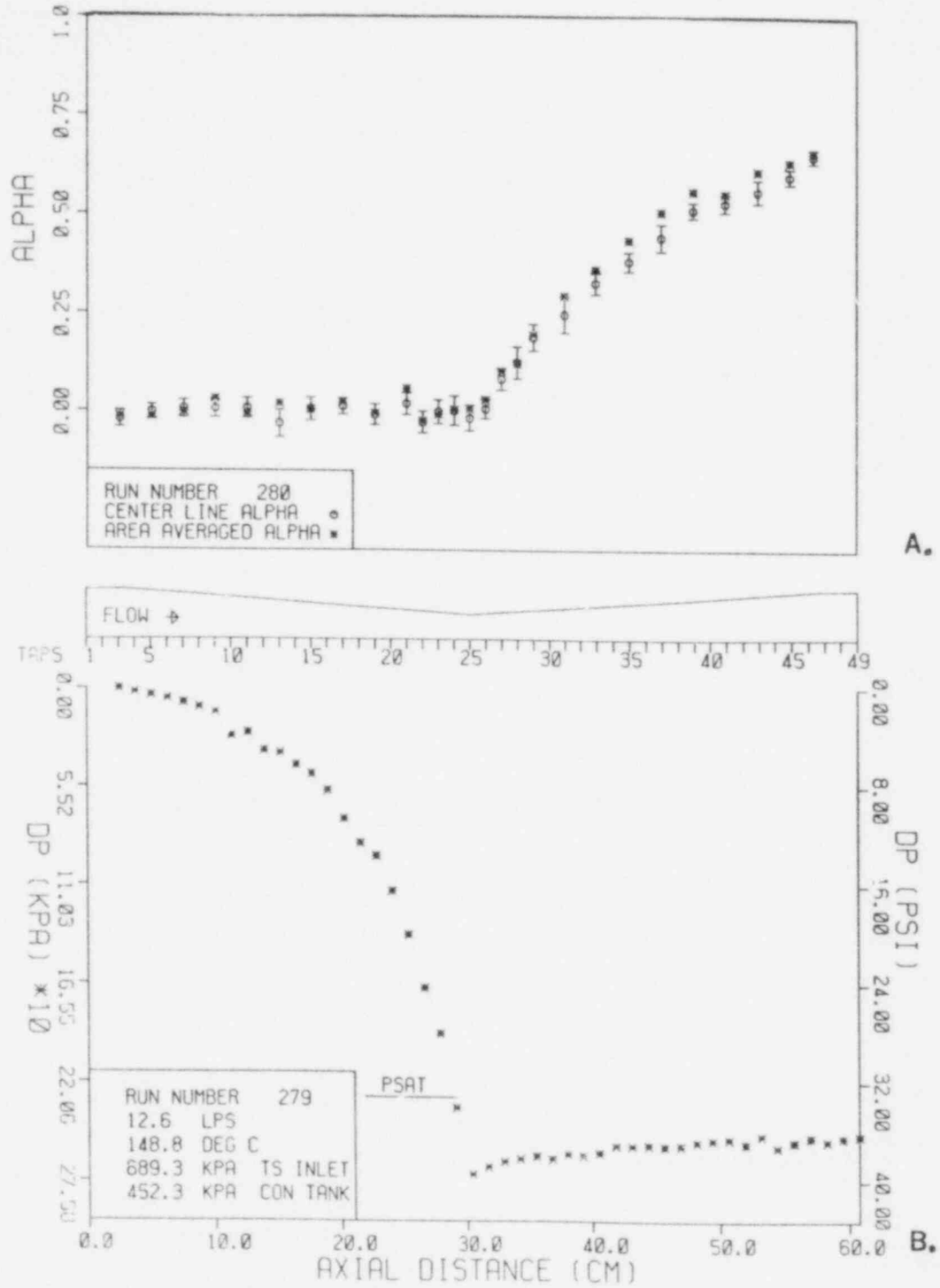

Figure 1.11. Axial distributions of the area-averaged and the center line diametral void fractions (A) and of the pressure drop (B) in the test section. Runs 279 and 280 were performed under the following conditions: p_{in}= 689.3 kPa, T_{in}= 148.8 C, p_{ct}= 452.3 kPa and at a mass flow rate of 11.6 kg/s. (BNL Neg. No. 6-950-80).

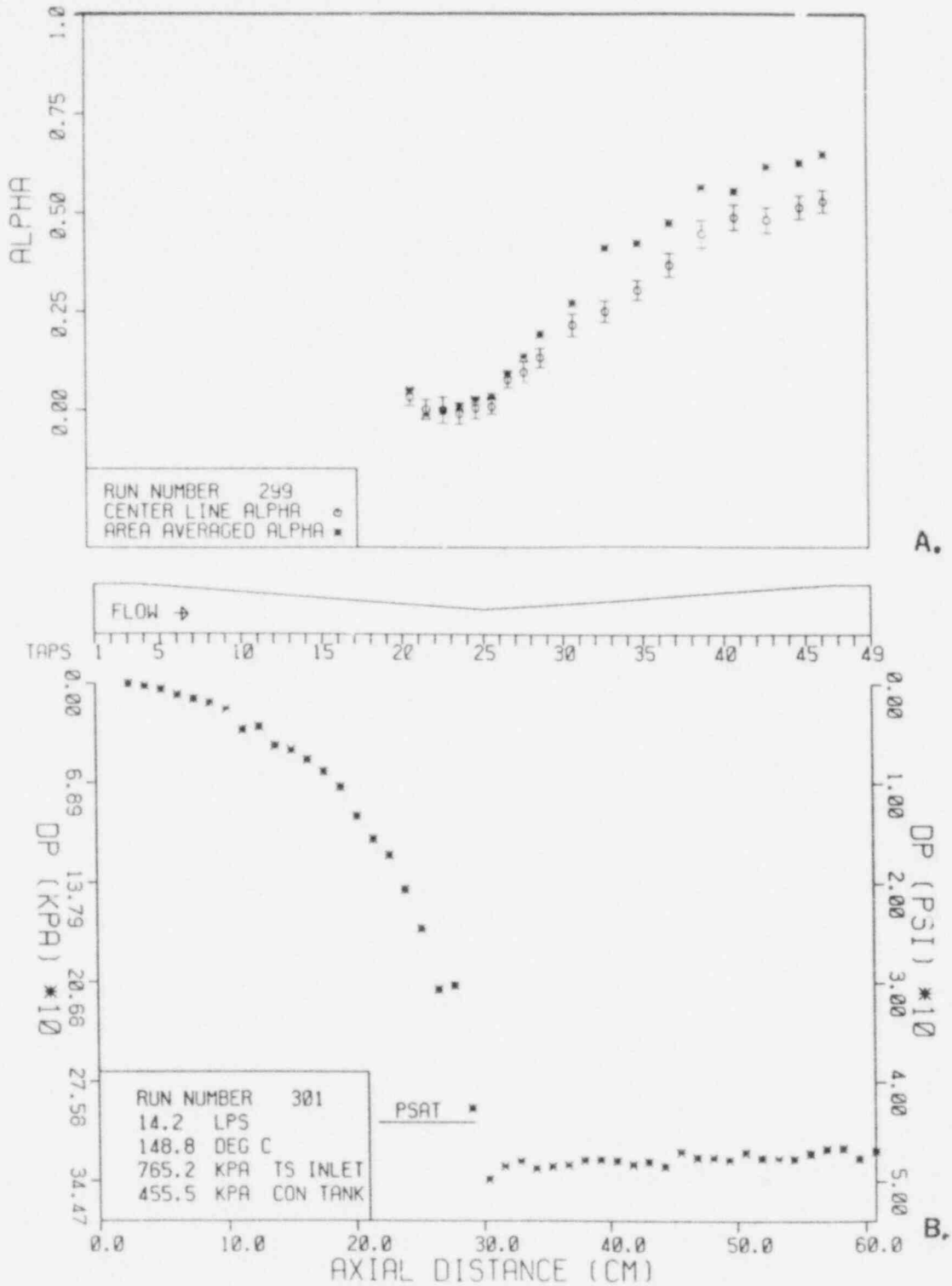

Figure 1.12. Axial distributions of the area-averaged and the center line diametral void fractions (A) and of the pressure drop (B) in the test section. Runs 299 and 301 were performed under the following conditions: p_{in}= 765.2 kPa, T_{in}= 148.8 C, p_{ct}= 455.5 kPa and at a mass flow rate of 13.1 kg/s. (BNL Neg. No. 6-956-80).

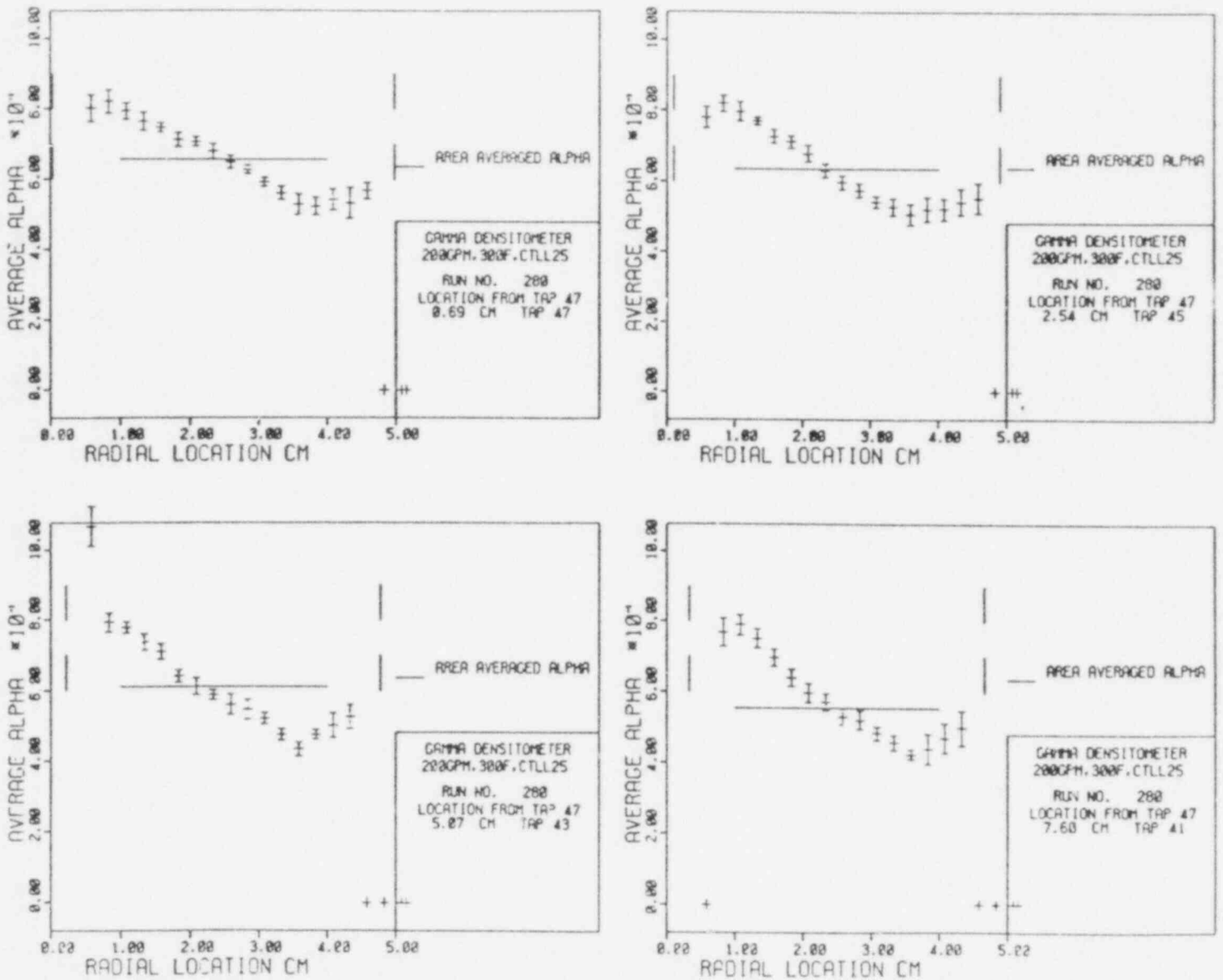

Figure 1.13. Transverse distributions of the chordal-averaged void fractions at axial locations corresponding to pressure taps 47, 45, 43 and 41 for Run 280 presented in Figure 1.11. (BNL Neg. No. 6-948-80).

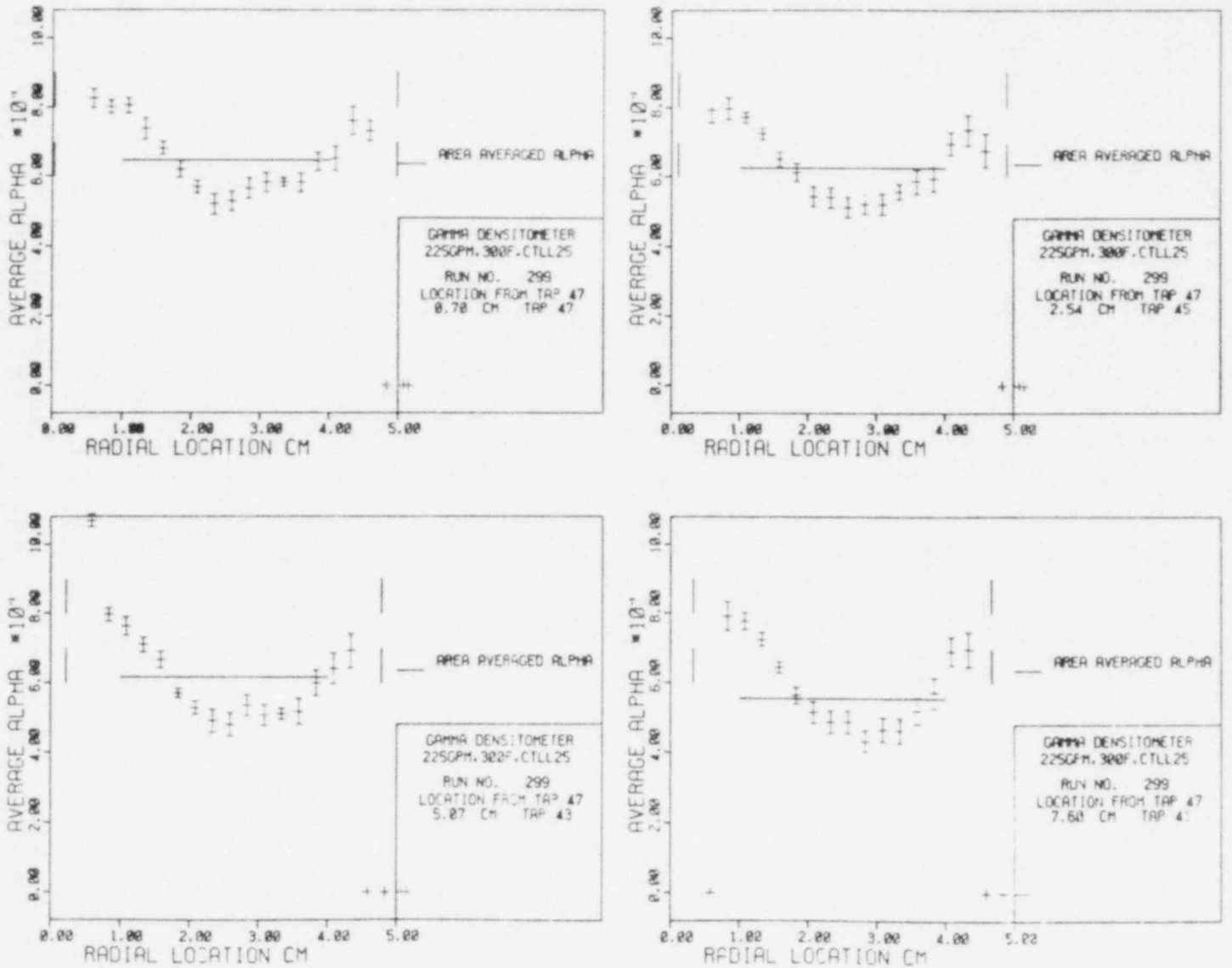

Figure 1.14. Transverse distributions of the chordal-averaged void fractions at axial locations corresponding to pressure taps 47, 45, 43 and 41 for Run 299 presented in Figure 1.12. (BNL Neg. No. 6-957-80).

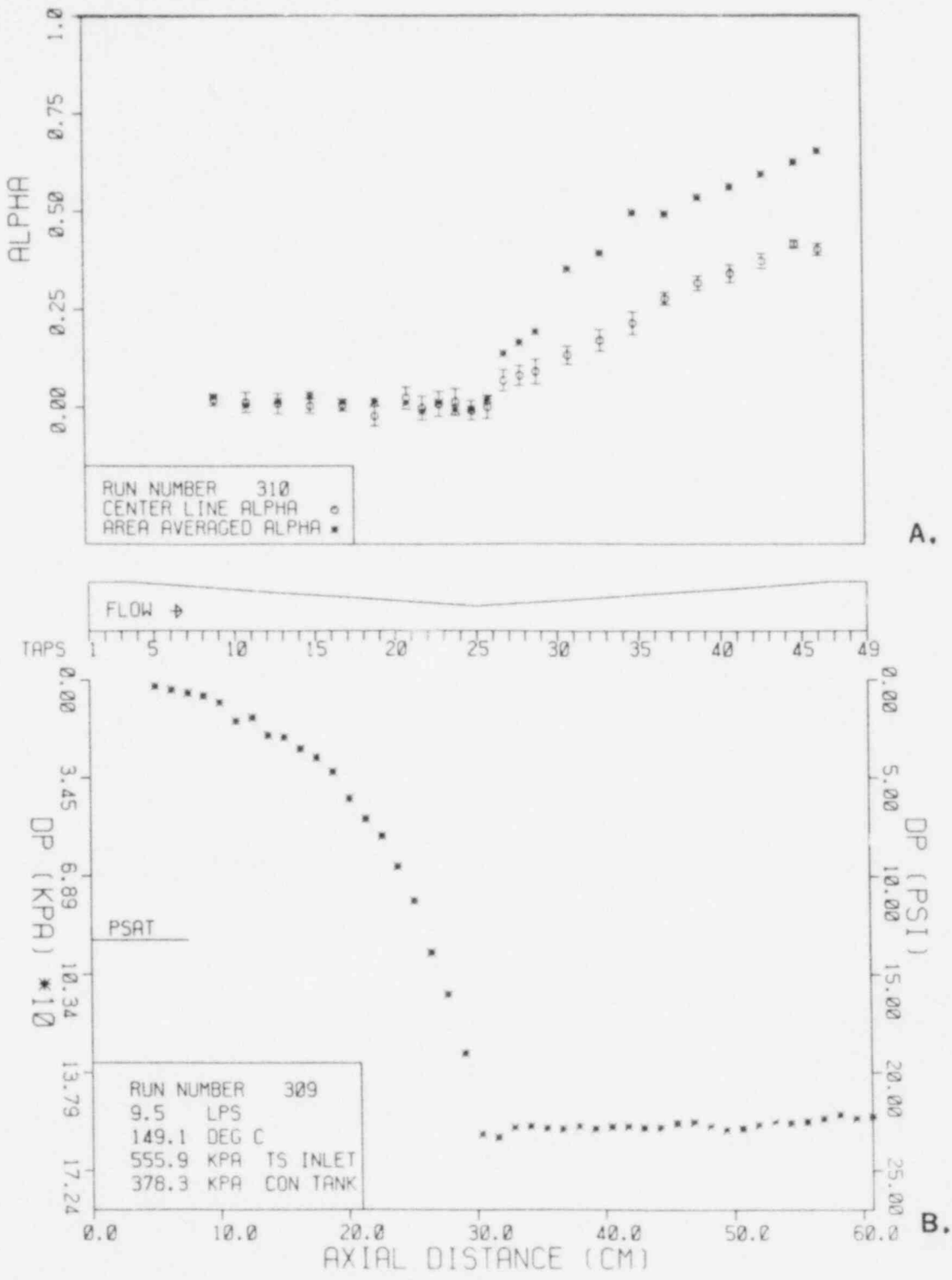

Figure 1.15. Axial distributions of the area-averaged and the center line diametral void fractions (A) and of the pressure drop (B) in the test section. Runs 309 and 310 were performed under the following conditions: p_{in}= 555.9 kPa, T_{in}= 149.1 C, p_{ct}= 378.3 kPa and at a mass flow rate of 8.8 kg/s. (BNL Neg. No. 6-955-80).

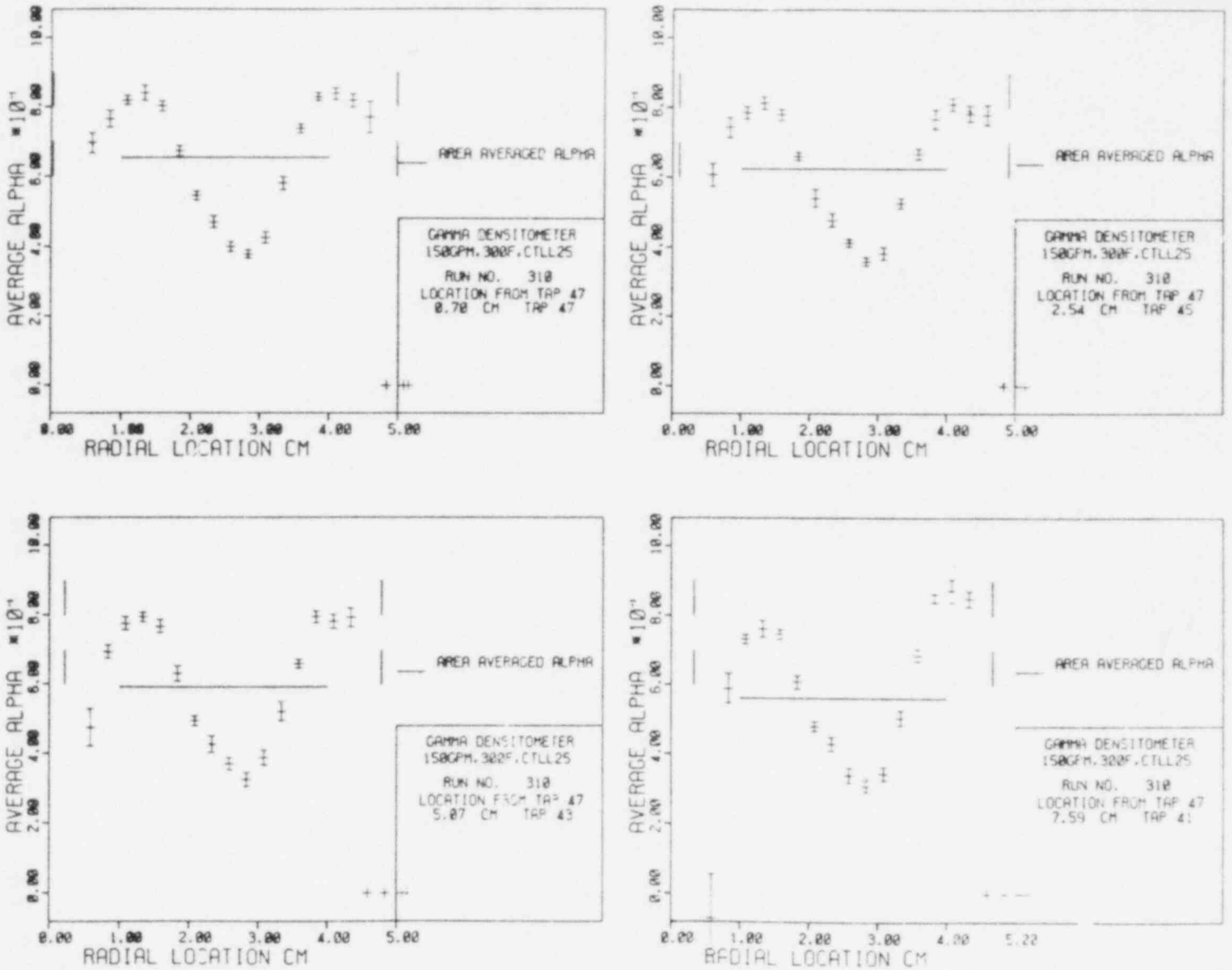

Figure 1.16. Transverse distributions of the chordal-averaged void fractions at axial locations corresponding to pressure taps 47, 45, 43 and 41 for Run 310 presented in Figure 1.15. (BNL Neg. No. 6-949-80).

Region	U_∞	Re_b range	ω range	n
1	$\frac{2\,\omega^2\,(\rho_\ell-\rho_g)\,g}{9\,\mu_\ell}$	$Re_b < 2$	$\omega < \left[\frac{9}{2}\,\frac{\nu_\ell^2}{(1-\rho_g/\rho_\ell)\,g}\right]^{1/3}$	2
2	$0.33\,g^{0.76}\,\nu_\ell^{-0.52}\,\omega^{1.28}$	$2 < Re_b < 4.02\,G_1^{-0.214}$	$\left\{9\,\nu_\ell^2/[2\,(1-\rho_g/\rho_\ell)g]\right\}^{1/3} < \omega < 2.21\,(\nu_\ell^2/g)^{1/3}\cdot G_1^{-0.0939}$	1.75
3	$1.35\sqrt{\frac{\sigma_\ell}{\rho_\ell\,\omega}}$	$4.02\,G_1^{-0.214} < Re_b < 2.59\,G_1^{-0.25}$	$2.21\,(\nu_\ell^2/g)^{1/3}\cdot G_1^{-0.0939} < \omega < 0.918\sqrt{\sigma_\ell/(\rho_\ell\,g)}$	1.75
4	$1.41\left[\frac{g\,\sigma_\ell(\rho_\ell-\rho_g)}{\rho_\ell^2}\right]^{1/4}$	$Re_b > 2.59\,G_1^{-0.25}$ and $\omega < 2\sqrt{\sigma_\ell/(\rho_\ell\,g)}$	$0.918\sqrt{\sigma_\ell/(\rho_\ell\,g)} < \omega < 2\sqrt{\sigma_\ell/(\rho_\ell\,g)}$	1.5
5	Same as 4	$\omega > 2\sqrt{\sigma_\ell/(\rho_\ell\,g)}$	$\omega > 2\sqrt{\sigma_\ell/(\rho_\ell\,g)}$	0

TABLE 1.1. Bubble Rise Velocities. where ω is the equivalent sphere radius of the bubble $\equiv (3\,V/4\,\pi)^{1/3}$,

ν_ℓ is the kinematic viscosity of the liquid $\equiv \mu_\ell/\rho_\ell$,

$Re_b \equiv 2\,\rho_\ell\,V_\infty\,\omega/\mu_\ell$, $G_1 \equiv g\,\mu_\ell^4/(\rho_\ell\,\sigma_\ell^3)$.

Region*	T = 120°C	T = 300°C	T = 350°C
1	ω_b < 30 μm U_∞ (30 μm) = 8.4 mm/s	ω_b < 20 μm U_∞ (20 μm) = 6.4 mm/s	ω_b < 21 μm U_∞ (21 μm) = 6.0 mm/s
2	30 μm < ω_b < 0.64 mm U_∞ (30 μm) = 8.2 mm/s U_∞ (0.64 mm) = 41.5 cm/s	19.4 μm < ω_b < 0.39 mm U_∞ (19.4 μm) = 6.7 mm/s U_∞ (0.39 mm) = 31 cm/s	19 μm < ω_b < 0.28 mm U_∞ (19 μm) = 6.6 mm/s U_∞ (0.28 mm) = 21 cm/s
3	0.66 mm < ω_b < 2.2 mm U_∞ (0.66 mm) = 40. cm/s U_∞ (2.2 mm) = 21.8 cm/s	0.4 mm < ω_b < 1.3 mm U_∞ (0.4 mm) = 30 cm/s U_∞ (1.3 mm) = 16.7 cm/s	0.29 mm < ω_b < 0.74 mm U_∞ (0.29 mm) = 20. cm/s U_∞ (0.74 mm) = 12.5 cm/s
4	2.2 mm < ω_b < 4.9 mm U_∞ = 21.8 cm/s	1.3 mm < ω_b < 2.9 mm U_∞ = 16.7 cm/s	0.74 mm < ω_b < 1.6 mm U_∞ = 12 cm/s
5	ω_b > 4.9 mm	ω_b > 2.9 mm	ω_b > 1.6 mm
	Same as Region 4		

TABLE 1.2. Free Rise Velocities of Steam Bubbles in Water.

α range	h	$V_{g\ell}$	A_s
α_o Inception	$h = h_{P.Z.} = \sqrt{3\, k_\ell \rho_\ell C_{p\ell}/\pi\, t}$	0	$\alpha_o = 0.0397\ (C_\Gamma R_{cr})^3$ $A_{so} = 3\alpha_o/R_{cr}$
α_o ↓ $\alpha_{b\,max}$ Bubbly Flow	$h = h_{P.Z.} \cdot f\ (V_{g\ell}\ t/\omega)$ $f(\xi) = \sqrt{1+C_1\xi/3}$ (Aleksandrov) $f(\xi) = 1+\sqrt{C_1\ \xi/3}$ (Wolfert) C_1 = 2 for spheres, 2.88 for spherical caps. Transition in regions 3 & 4 in Table 1.1.	$V_{g\ell} = V_{g\ell}\ (Re_b)$ or $V_{g\ell}\ (\omega)$ for bubbles, 5 formulas for 5 Re_b or ω ranges - See Table 1.1.	$A_{s,b} = 3\ \alpha/\omega$ where ω from $\frac{d\omega}{dt} = \frac{\dot{q}''_b}{L\ \rho_g}$
$\alpha_{b\,max}$ ↓ $\alpha_{s\,max}$ Bubbly-Slug Flow	$h \cdot A_s = h_b \cdot A_{s,b} + h_T \cdot A_{s,T}$ $h_b = h_{P.Z.} \cdot F\left(\frac{V_{g\ell}\ t}{\omega}\right)$ (as in bubbly flow) $h_T = 0.0073\ \rho_\ell\ V_{g\ell}\ C_{p\ell}$	$V_{g\ell} = (\alpha_b\ V_{g\ell,b} + \alpha_T\ V_{g\ell,T})/\ \alpha$ where $V_{g\ell,b}$ as in bubbly flow above $V_{g\ell,T} = \frac{0.35}{1-\alpha}\sqrt{\frac{g(\rho_\ell-\rho_g)\ D}{\rho_\ell}}$ where $\alpha_b^{\ 1}$ = const = $\alpha_{b\,max}$, $\alpha_T = (\alpha-\alpha_b^{\ 1})/(1-\alpha_b^{\ 1})$, $\alpha_b = (1-\alpha_T)\alpha_b^{\ 1}$, λ = length-diameter ratio of Taylor bubbles & unit cells.	$A_{s,b} = 3\alpha_b/\omega$, ω from $d\omega/dt = \dot{q}''_b/L \cdot \rho_g$ $A_{s,T} = 4\ \alpha^{2/3}\ [(1/2\ \lambda) + 1]/\ D$
$\alpha_{s\,max}$ – α_d Transition Annular – Mist Flow	Linear interpolation with respect to α between bubbly-slug and drop flows.		Linear interpolation with respect to α between bubbly-slug and drop flows.
α_d ↓ 1.0 Droplet Flow	$h_d = (2.0+0.74\ Re_d^{1/2} Pr_g^{1/3})k_g/d$ where $Re_d = \rho_g\ V_{g\ell}\ d/\mu_g$ $Pr_g = C_{pg}\ \mu_g/k_g$	$V_g = \frac{1.4}{\alpha}\left[\frac{g\ \sigma_\ell\ (\rho_\ell-\rho_g)}{\rho_g^{\ 2}}\right]^{1/4}$	$A_{s,d} = 6\ (1-\alpha)/d$ $d = We_{d,cr}\ \sigma_\ell/\rho_g\ V_{g\ell}^{\ 2}$

TABLE 1.3. Summary of Formulas. where ω = equivalent sphere radius of bubbles, d = droplet diameter, D = pipe diameter, L = latent heat. Other symbols see text.
Recommended values: $\alpha_{b\,max} = 0.3$, $\alpha_{s\,max} = 0.8$, $\alpha_d = 0.95$, λ = 4 or 5, $We_{d,cr} = 12$.

2. RAMONA-III Code Modification and Evaluation

An assessment was completed of how RAMONA-III might be used for analysis of small pipe break LOCAs in LWRs. The code currently is not able to do such calculations although it already has several features which make it an attractive candidate. Our study has given us an understanding of what modifications are necessary to be able to give us this capability. Tests which will help determine how much effort is necessary have been identified. Work has started on modifications which will allow the code to bypass the neutronics calculation in order to improve running time. Work also began on running problems with flow going out the feedwater inlet in order to test the level tracking in the downcomer.

A review of other plant transients was made in order to recommend additions to the plant protection system modelling in RAMONA-III. Work began on implementing the algorithms for calculating reactivity components.

2.1 RAMONA-III Small Break LOCA Calculational Capability

2.1.1. General Requirements of Small Break Analysis

For the standard small break LOCA licensing analysis, several conservative assumptions are made which exaggerate the severity of the accident. The most limiting single active failure is assumed, which usually leads to the assumption of loss of the high pressure ECC system. Also the high drywell pressure signals are neglected and the reactor is scrammed and the containment is isolated on the low water level signal. This assumes a minimum vessel inventory at the start of the transient. Feedwater flow, control rod drive flow and offsite power are assumed unavailable. Additionally, no credit is taken for the RCIC system or any operator action for the first ten minutes. The result of all these assumptions is that all high pressure coolant systems are disabled, requiring vessel depressurization to allow the low pressure systems to reflood the vessel. These assumptions make the standard analysis very conservative since the normal high pressure coolant systems are more than adequate to maintain water level.

A computer code which analyzes all small break transients must adequately evaluate the system depressurization, energy loss, and total inventory. In addition the distribution of inventory must be obtained, particularly in the downcomer where the level trip signals originate.

In order to accomplish these goals the code must contain specific geometric and modeling features. Axial noding must be sufficient for accurate calculation. It must be possible to model a separate bypass channel since the control rod drive flow enters this channel and also since the possibility exists for flow in opposite directions in the core and bypass channels. Separate average and hot channels should also be modeled in order to calculate peak clad temperature.

Since the duration of a small break transient can be as long as 6×10^3s, the running time of the code should be on the order of real time.

The possible break locations include both the suction and discharge legs of the jet pump recirculaton lines. This makes it desirable that the code have at least two separate jet pump recirculation loops; one to represent the intact loops and one to represent a possibly broken loop. With this arrangement it may also be necessary to have two associated downcomers to model asymmetric conditions resulting from a recirculation line break. The jet pump recirculation model should also be capable of calculating two phase and reverse flow conditions in the event of a recirculation line break or in case the jet pump becomes uncovered due to a break at another location.

Another necessary capability of the code is the tracking of the mixture level as inventory is lost through the break or replaced by the safety systems. In the downcomer an accurate calculation is required since the level trips which activate the safety systems are located in this region. It is necessary to calculate the degree of uncovery of the core in order to determine the proper heat transfer regimes for determining cladding temperatures.

The code must contain an appropriate model of the break itself so that the proper mass and energy loss can be determined. This break model must be capable of calculating breaks at the following locations:

- Recirculation suction line
- Recirculation discharge line
- Steamline
  - Inside containment
  - Outside containment
- Core spray line
- Feedwater line
- Control rod drive line
- Incore monitor vessel penetrations
- Drain lines
- Standby control lines

The safety and control systems must also be modeled by the code. This includes logic for actuations on appropriate signals and a modeling of the flow rate and energy delivered to the proper location for each system - which can vary for different BWR designs. These systems include:

- Scram
- High pressure core spray/high pressure coolant injection (HPCS/HPCI)
- Recirculation flow restrictors
- Main steamline isolation valve (MSIV)
- Control rod drive (CRD)
- Low pressure core spray (LPCS)
- Low pressure coolant injection (LPCI)
- Automatic depressurization system (ADS)
- Safety relief valves (SRV)
- Reactor core isolation cooling/ isolation condenser (RCIC/IC)

2.1.2 Present Capabilities

The present version of the RAMONA-III code already has some of the capabilities for small break analysis mentioned in the preceding section. Some are sufficient as they exist, while others require testing and possible improvements. Still other capabilities are not present at all and require additions to the code.

The present RAMONA-III code has a level tracking model for Downcomers 1 and 2 and Lower Plenum 1. This model basically compares the total system inventory volume to the geometric volume of the system, ignoring the mass of vapor above the level. This model has not been tested and its limits are unknown. In the core and riser no level tracking capabilities exist. However, the code calculates the void fraction as a function of time and space at each node. The knowledge of the local void may be sufficient to determine the proper heat transfer to calculate the cladding temperature.

The RAMONA-III noding and core channel capability is sufficient for small break analysis. Up to 24 axial nodes are allowed in the core and an adequate number of nodes are available in the other reactor sections. A separate bypass channel is provided and up to 45 active core channels are available.

Reverse flow capability has been provided in the main loop. However, this has never been tested. A single jet pump, recirculation line model presently exists. However, this model is only adequate for single-phase, unidirectional flow.

The code presently computes the clad temperature. However, only two heat transfer regimes are available.

The code calculates two-phase nonequilibrium flow with a slip and bubble rise velocity model. A condensation/evaporation model is included, however, condensation above the liquid level in the downcomer is not provided for.

2.1.3. Tests, Additions and Modifications Proposed for RAMONA-III

As mentioned in the previous section RAMONA-III has a level tracking capability in the downcomer and lower plenum regions. It is proposed to test the limits and acceptability of this model. In the rest of the main loop tests will be run to determine if the use of the presently calculated void profile is sufficient for determining the level. If this is not the case a new model will have to be added. This will require complex computer coding.

An additional jet pump, recirculaton loop may have to be added and solved simultaneously with the existing loop. Reverse flow and two phase flow capability may have to be added to both loops. The possibility of an additional downcomer will be investigated and added if required.

A break model sufficient to deal with the breaks listed in Section 2.1.1 will be required. Control and protection system trip signals must be added for the following systems:

HPCS/HPCI
LPCS/LPCI
RCIC
CRD
ADS (Automatic Depressurization System)
MSIV (Main Steam Isolation Valve)
SRV (Safety and Relief Valves)

The MSIV and SRV are already modelled in the code; however, the other safety system models must be developed. These must deliver the proper flow and energy at the proper location. This includes injection models for HPCI, LPCI, CRD, and RCIC. A core spray model for the HPCS and LPCS systems must be developed. This must include the capability of injecting cold water into a vapor region. The core spray also requires the capability of calculating countercurrent flow limitation (CCFL) when cold water is sprayed into a rising steam flow. Finally, a reflood model may be required. These are also complex problems.

In the basic RAMONA-III modeling various items must be looked at. First the present reverse flow capability must be tested to see if it works and if the model is adequate. This is also true of the two-phase capabilities in the downcomer; all calculations to date have only had pure liquid in the downcomer.

More heat transfer regimes, including radiative heat transfer, will have to be added to cover higher void flows.

A question which needs investigation is the need for representating superheated steam. RAMONA-III presently assumes all steam is saturated. Requiring this capability would mean the addition of an energy equation to the code - a complex task.

In the spray cooling regime it may be necessary to calculate local pressure changes or even acceleration terms. RAMONA-III presently computes all properties at one system pressure.

A decay heat model currently exists which has never been tested. The decay heat is calculated in conjunction with prompt heat which is calculated from the three dimensional neutronics. For a small break, only point kinetics or an input power versus time function may be needed. The axial power distribution would be obtained from input for a small break. The code must be modified in order to allow for this means of heat generation.

Finally, after all additions and a proper geometric configuration is developed, the running time vs. real time must be evaluated and measures taken to speed up the code if necessary or possible.

2.1.4. Power Generation Input Capability

In order to do small break analysis RAMONA-III is first being modified to be able to read a table of nuclear power vs. time. It will then be able to calculate the heat transfer from the fuel to the coolant and the thermal-hydraulics of the coolant without doing any neutronic calculations. This table could be read in before the calculation of the steady state or before the calculation of the transient.

In order to achieve this capability, work is proceeding in several steps. The first step, completed this quarter, has been to stop the neutronics after the calculation of the steady state and to do the hydraulics with a table of thermal power (i.e., power to the coolant) vs. time. The second step is to add the heat conduction section of the code to the first step, so that a nuclear power table can be read in. The code will calculate its own thermal power and then the hydraulics. The third step will be to eliminate the neutronics from steady state calculations as well, i.e., make the second step operational for steady state calculations.

2.1.5 Level Tracking Tests

A series of runs have begun which are to examine the present small pipe break capabilities of the RAMONA-III code. These studies are to investigate: a) level tracking in the downcomer, b) void profile in the core, c) reverse flow, d) two-phase in the downcomer, and e) running time.

To improve running time a coarse representation of the Peach Bottom-II reactor (TT3 state) was constructed. The representation had four neutronic channels and two hydraulic channels plus bypass. Runs have been made to establish and then investigate a level in the downcomer.

The longest run to date has been a run representing 13.5 reactor seconds where the level dropped to -5.01m (from downcomer top). During this run the system pressure had been held constant. The neutronics have been scrammed at zero time. After a couple of seconds a constant power asymptote consistent with the contant decay heat model and present input is reached. The feedwater was ramped between 0.1 and 0.2s to the negative of the steady state flow (i.e. flow out the feedwater pipe). Shortcomings in the code which used input parameters for the feedwater to compute the enthalpy of the outgoing water were corrected. This problem manifested itself in an erroneous heating of the node with the feedwater pipe entrance. Problems have been identified in the logic (for both positive and negative feedwater flow) when the water level falls below the feedwater node. The feedwater contribution to the mass flow appears to be present but the contribution to the energy equation is omitted when the water level is below the feedwater node. Questions of modelling what void should flow out the feedwater pipe once the level has dropped below its entrance remain.

In this run the water level was initially placed at -3 meters. A 2 meter level drop was observed. Two-phase flow was observed in the downcomer in that void was created below the water level and evaporation and temperatures above saturation were encountered. What was observed can best be characterized as

the "sweeping out" of the steady state fluid with the cutting off and reversing the feedwater. Return fluid at temperatures slightly above saturation continues to fall back from the upper plenum.

A level was not established in the core nor was it expected. With constant imposed pressure, decrease in power to 10% and the pump still running the average void fraction in the core approached 0.09 with an exit value of 0.18.

The running time for the four neutronic/three hydraulic channel configuration to calculate 13.5 seconds of reactor transient took just under 200 cp seconds on the CDC-7600. The calculation took 339 neutronic steps of which once the neutronics scrammed most of the calculation proceeded at maximum step size of 0.1 seconds. It should be noted that the hydraulics takes smaller time steps than the neutronics and during the present run the neutronics (not counting the fuel heat transfer) took only 35% of the computing time.

2.2 RAMONA-III Plant Protection System

Chapter 15 of the General Electric Standard Safety Analysis Report was reviewed in order to determine what additional features of the plant protection system should be added to the code. The additions would allow more plant transient scenarios to be analyzed. Note that large or small break LOCAs were not considered. A memo was written listing the recommended additional trips.

Three system activations based on several trip signals were recommended as listed below:

I. Safety/Relief Valve Opening/Closing

1. Time (manual action)
2. Steamline pressure too high/low

II. Closure of Main Steam Isolation Valve

1. Low steam pressure
2. High steamline flow
3. Low vessel water level
4. Time (manual action)

III. Turbine Stop Valve Closure

1. Low system pressure (in order to simulate the presence of a pressure regulator model).

2.3 RAMONA-III Reactivity Components

The problems involved in implementing reactivity edits into the RAMONA-III code have been studied. Reactivity edits have been previously implemented in the BNL codes BNL-TWIGL and MEKIN-B. These implementations have been looked at to learn the similarities and focus the differences encountered in RAMONA-III. The mathematical expressions for the adjoint fluxes, which are necessary for the reactivity calculations, have been formulated in terms of the RAMONA-III neutronic equations.

3. IRT Code Modification and Evaluation

3.1 Once-Through Steam Generator Modeling Mark II Version

Preliminary calculations have been obtained using the Mark II once-through steam generator model in the IRT code. These results are now being compared with results obtained for a similar transient using the Mark I version.

3.2 Once-Through Steam Generator Analysis

The analysis of the overcooling transient for a typical B&W plant has continued. Current work is involved in several sensitivity studies including a variation in the control rod worth and in the amount of steam flow out the secondary side bypass system.

3.3 Loop Momentum Equation

A loop momentum equation is being incorporated into the IRT code to allow calculation of such cases as natural circulation and pump trip. Results have shown that an implicit integration of the momentum equation is accurate and stable. The inclusion of the pump model into the system equations has been started.

3.4 RETRAN Code Implementation and Verification

Two input data decks have been obtained from the Tennessee Valley Authority that represents the Sequoyah plant. These input decks have been run with the RETRAN code on the BNL CDC-6600. In addition, the plant models have been modified to represent the first of a series of natural circulation tests that are planned for the Sequoyah plant. These results have been transmitted to NRC staff. The results provide some indication of the natural circulation capability of the plant during the test.

4. TRAC Assessment and Model Development

4.1 Moby-Dick Nitrogen-Water Tests (P. Saha)

A number of these tests (Jeandey, 1979) have been rerun with TRAC-P1A using the "corrected" single-phase friction factor values. As shown in Figure 4.1, this has been achieved by increasing the values for the smooth wall, Blasius-type friction factor by 5 percent in the homogeneous and the Armand friction factor options. However, for the annular and the Chisholm correlations, which use a rough-wall, Colebrook-type single-phase friction factor, the "corrected" values are obtained by specifying a lower value (1×10^{-6}m) for the roughness heights than that built into the code (5×10^{-6}m). These modifications have resulted in smaller differences among the TRAC-P1A predictions of water flow rates for different two-phase friction factor options, as evidenced by Table 4.1. For the original TRAC-P1A, the differences between the predicted water mass flow rates by the annular and the homogeneous friction factor were about 20 percent (Saha, 1980). The results thus show the importance of using the same single-phase friction factor correlation for all two-phase friction factor options available in the code. It is recommended that in the future version of TRAC, only the Colebrook-type single-phase friction factor be retained with user-input roughness parameter.

Assessment of TRAC-P1A by using the Moby-Dick nitrogen-water tests is now complete. A report on this activity will be prepared soon.

4.2 University of Houston Counter-Current Flow Test (U. S. Rohatgi)

The test facility (Dukler, 1977) consists of a vertical tube in which water is introduced through a porous section and the air flows in at the bottom. The liquid film is very thin and the void fraction is greater than 90 percent throughout the test section. Therefore, simulation by the TRAC-P1A 1-D formulation will use a relative velocity for annular flow regime. However, it is found that this description of a relative velocity will always yield gas and liquid velocities in the same direction as shown her ,

$$V_r = \frac{V_m}{\left[\frac{\rho_g (76 - 75\alpha)}{\rho_\ell \sqrt{\alpha}}\right]^{\frac{1}{2}} + \frac{\alpha \rho_g}{\rho_m}}$$

so

$$V_\ell \left[1 + \left\{\frac{\rho_g (76 - 75\alpha)}{\rho_\ell \sqrt{\alpha}}\right\}^{\frac{1}{2}}\right] = \left[\frac{\rho_g (76 - 75\alpha)}{\rho_\ell \sqrt{\alpha}}\right]^{\frac{1}{2}} V_g$$

therefore, TRAC-P1A will not predict counter-current flow in the annular regime, and these tests cannot be simulated by the TRAC-P1A drift-flux formulation.

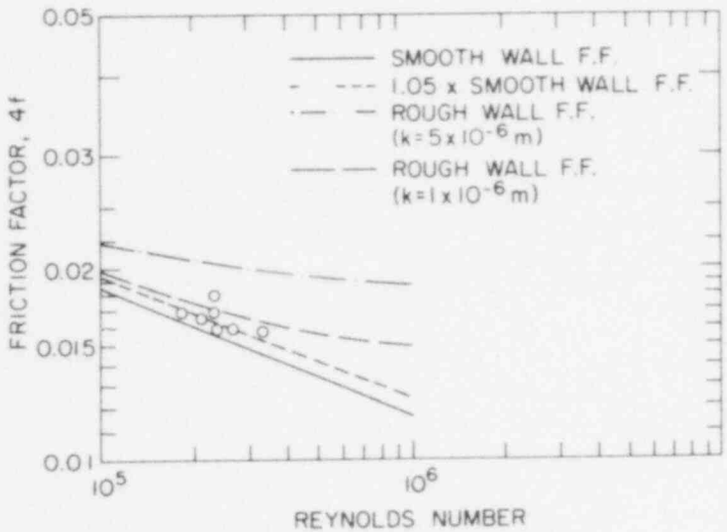

Figure 4.1 Comparison of the Single-Phase Water Calibration for Moby-Dick Test Section with Various Friction Factors. (BNL Neg. No. 7-112-80).

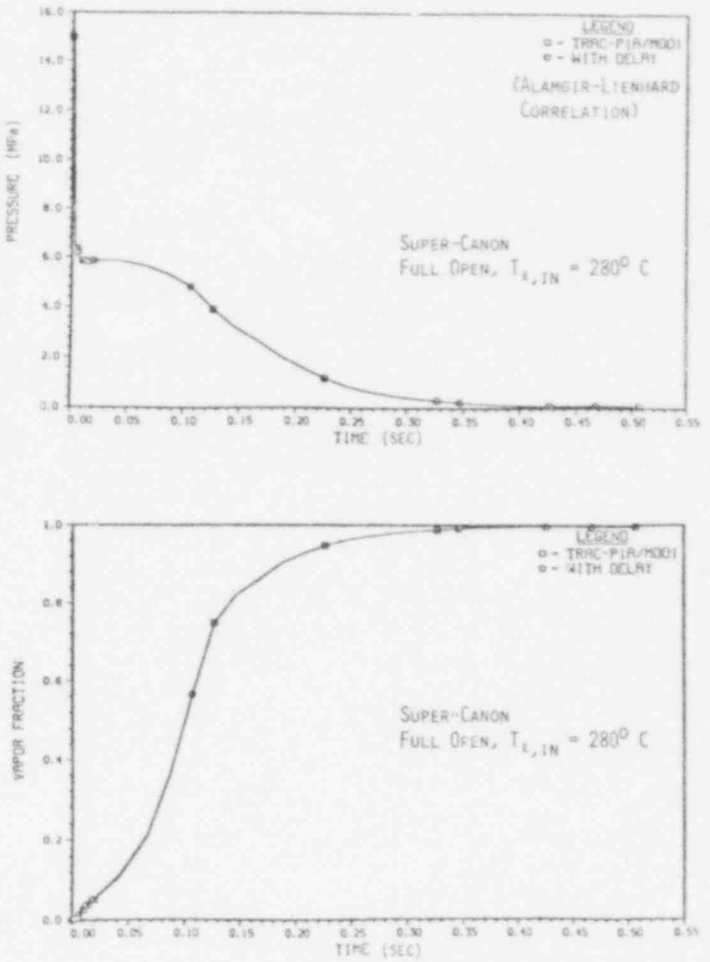

Figure 4.2 Comparison of TRAC-P1A Predictions of Pressure and Void Fraction for Super-CANON test with and without the Nucleation Delay Correlation of Alamgir and Lienhard. (BNL Neg. No. 7-113-80).

TABLE 4.1 SUMMARY OF MOBY-DICK RESULTS WITH "CORRECTED" SINGLE-PHASE FRICTION FACTORS

RUN NO.	MEASURED FLOW QUALITY (X)	WATER MASS FLOW RATE (kg/s)				
		EXPT.	TRAC CALC. (ANNULAR F.F.)	ERROR (%)	TRAC CALC. (HOMOGENEOUS F.F.)	ERROR (%)
3095	0	1.912	1.932	1.1	2.045	6.9
3176	0.94×10^{-4}	2.057	2.053	-0.2	2.184	6.2
3177	0.93×10^{-4}	2.063	2.109	2.2	2.213	7.3
3087	5.91×10^{-4}	1.915	2.019	5.4	2.198	14.8
3089	5.90×10^{-4}	1.918	2.027	5.7	2.200	14.7
3091	5.95×10^{-4}	1.915	2.024	5.7	2.196	14.7
3141	51.3×10^{-4}	1.222	.....DID NOT CONVERGE TO A STEADY-STATE.....			
3167	0.75×10^{-4}	2.634	2.661	1.0	2.790	5.9
3052	8.72×10^{-4}	1.929	2.044	6.0	2.235	15.8

4.3 Super-CANON Experiments (P. Saha and Y. Sanborn)

The sensitivity of TRAC-P1A predictions to relative velocity has been studied for a Super-CANON test (Riegel, 1979) with full-open discharge end and an initial water temperature of 280° C. This was performed by changing the value of void distribution parameter, C_o, from 1.1 to 1.01, which reduced the relative velocity or the slip between the phases, and the flow approached a homogeneous condition. This change in relative velocity did not significantly affect the short-term ($t < 0.1$ sec.) pressure history. However, the discharge flow rate was somewhat reduced, and thus the long-term ($t > 0.1$ sec.) pressure prediction was in closer agreement with the experimental data.

The same test was also simulated by the BNL-modified version of TRAC-P1A containing the correlation of Alamgir and Lienhard (1980) for nucleation delay. The correlation produced a pressure dip when the initial pressure wave moved from the discharge end to the closed end. However, as soon as the vapor generation started, the calculated pressure recovered to the original TRAC-P1A prediction, and thereafter remained almost at the same value as the earlier TRAC prediction. This is shown in Figure 4.2. Therefore, it is clear that the inclusion of a delayed flashing model cannot improve the TRAC predictions for the Super-CANON tests, and further examination of the TRAC models for nonequilibrium phase change and relative velocity is required.

4.4 Marviken Critical Flow Tests (U. S. Rohatgi and Y. Sanborn)

In the last quarterly (Rohatgi 1980a), Marviken critical flow tests with nozzle diameter of 0.5 m were predicted. In the current quarter the remaining tests (25, 26) with smaller nozzle diameter (0.3 m) were simulated with TRAC-P1A. These tests have an L/D of 1.7, and initial subcooling of 6° C and 30° C (Ericson, 1979). Figure 4.3 shows the ratio of the predicted to experimental pressure values at the top of the vessel. Here, as expected, the errors are greater in the Test 26 predictions, which have larger subcooling than in Test 25. However, the mass flow rate prediction behaves differently as shown in Figure 4.4. This larger error in the mass flow rate prediction in the case of Test 25 could be attributed to a larger error in the density measurements which had at best a 12 percent accuracy for the two-phase flow condition when all three beams are working. Even in subcooled conditions, Test 25 has larger error than Test 26. However, these results also show that TRAC-P1A underpredicts the mass flow rate in the long term.

It has been found that TRAC-P1A could not predict the initial pressure undershoot ($t < 2$ sec.) in any of the tests. This is due to the lack of a delayed flashing model in the code. This has been corrected at BNL by incorporating into the code the Alamgir-Lienhard (1980) correlation for delayed flashing. A significant improvement in the pressure prediction for $t < 2$ sec. as shown in Figure 4.5 was obtained. This figure compares the pressure prediction for Test 24, as computed with the original TRAC-P1A and with the modified version containing the Alamgir-Lienhard correlation. The mass flow rate prediction, however, has not improved except for $t < 0.1$ sec., and the reasons for this are being investigated.

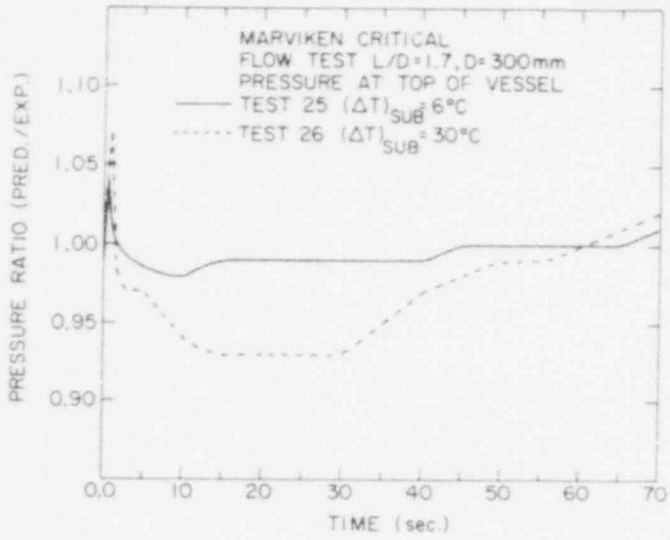

Figure 4.3 The Ratio of Predicted and Experimental Values of the Pressure at the Top of the Vessel. (BNL Neg. No. 6-1051-80).

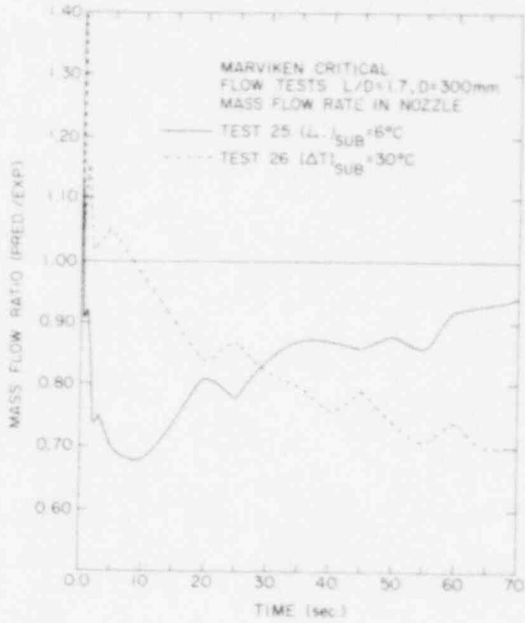

Figure 4.4 The Ratio of Predicted and Experimental Values of Mass Flow Rate at the Nozzle Exit. (BNL Neg. No. 6-1044-80).

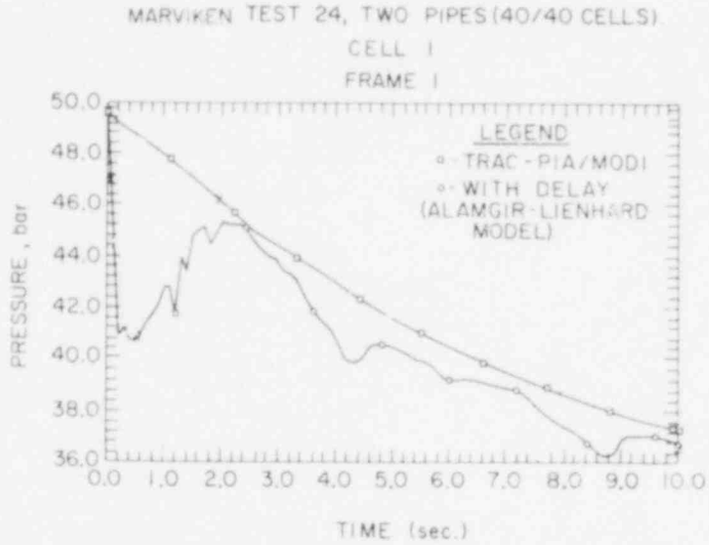

Figure 4.5 The Pressure at the Top of the Vessel as Predicted by TRAC-P1A With and Without Delay Model. (BNL Neg. No. 6-1043-80).

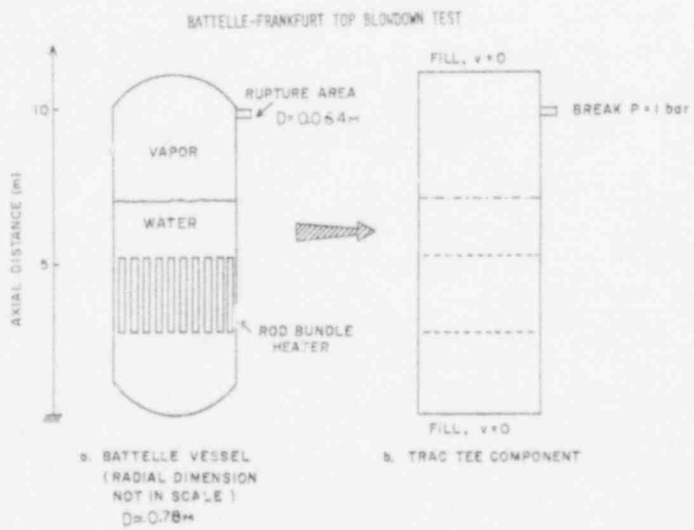

Figure 4.6 Battelle Vessel Configuration and Equivalent TEE Component for TRAC-P1A Computation. (BNL Neg. No. 6-1048-80).

4.5 Battelle Institute (Frankfurt-Main) Vessel Top Blowdown Test (L. Neymotin)

Simulation of this test (Holzer, 1977) has been performed using TRAC's "TEE" component (Figure 4.6) with two zero-flow "FILLS" at the TEE's top and bottom and with a pressure boundary condition at the free end of the secondary pipe accomplished by the "BREAK." In total, 120 nodes for the vessel (primary TEE pipe) and 10 for the discharge tube (secondary TEE pipe) were employed. The effect of the heater inside the vessel was taken into account by decreasing the flow area by 22 percent and the hydraulic diameter by approximately 10 times, compared to those for the vessel without the heater. The computations were done with the fully implicit option and required approximately two minutes on the CDC-7600 to cover the first three seconds of the blowdown.

Figure 4.7 shows the void, pressure, and temperature time history at the level of 6.35 m from the bottom. The pressure comparison is good except between t = 0.15 and 0.75 seconds where it is overpredicted by about 5 percent, apparently due to overprediction of the computed vapor generation rate. In addition, TRAC does not predict the slight pressure rise taking place in the experiment from the time of about 2.3 seconds after the two-phase mixture reaches the discharge nozzle. This rise can be explained by considering the jump in the amount of vapor leaving the vessel when the nozzle flow becomes two-phase. Figure 4.8 presents the mass flow rate and mixture level data. The area between the two mixture level curves corresponds to the two-phase region where the sharp jump in voids occurs.

The calculated mixture level reaches the nozzle more quickly than in the experiment; this could be caused by the present slip correlations implemented in TRAC. Assuming that the slip has been underestimated, a number of runs were made using different coefficients in the expression for the relative velocity, V_r. An increase of about 25 percent in the relative velocity has been found to yield the best fit. Corresponding results obtained with the modified TRAC's version are shown in Figures 4.7 and 4.8 as dashed curves. It is clearly seen to what extent the change in the slip modifies the time history of the two-phase boundary. The last TRAC result worth mentioning is the void fraction in the discharge nozzle which varied from 0.74 to 0.78 after the two-phase mixture had reached the nozzle level.

Because of possible inaccuracies in the temperature measurements, another computer run was performed to determine the sensitivity of the blowdown characteristics to variations in the initial water temperature. Unlike the previous runs with the initial water temperature constant everywhere in the vessel (285° C), the following temperature distribution has been chosen: from the bottom up to 3.75 m--280° C; up to 6.35 m--283° C; up to 7.07 m--285° C. These temperatures were selected from the temperature vs. time plots for different levels at time equals zero. It is seen from the results obtained at this time (Figures 4.9 and 4.10) that the mixture level time history is more reasonable than in the original run and is similar to the one obtained by modifying the "slip" subroutine in the TRAC P1A. On the other hand, the pressure in the vessel appears to be underpredicted.

All of this emphasizes the importance of knowing accurately the measured temperature fields in the vessel (in addition to the pressure) in order to utilize the data in TRAC assessment.

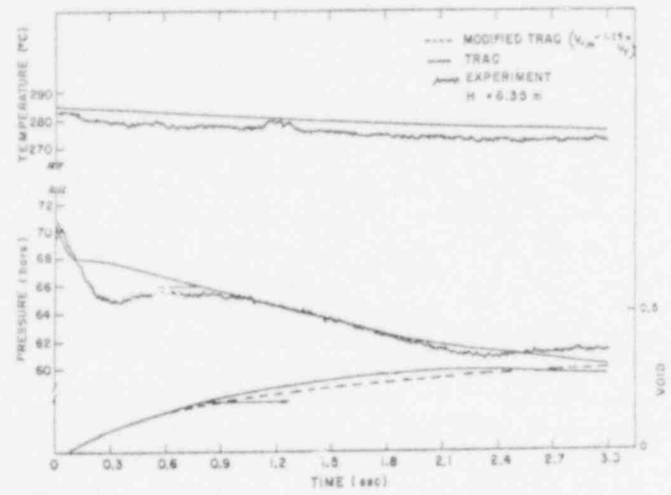

Figure 4.7 The Comparison of the Predictions of Temperature, Pressure, and Void Fraction by the Original and the Modified TRAC-P1A with Data. (BNL Neg. No. 6-1049-80).

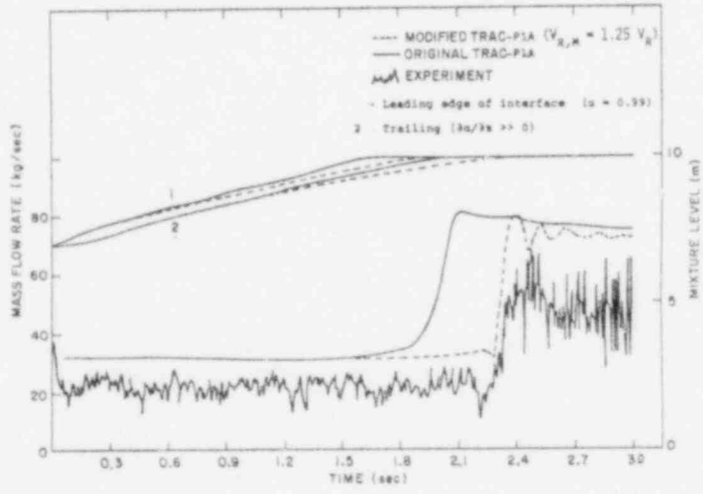

Figure 4.8 The Comparison of the Predictions of the Mass Flow Rate and the Mixture Level by the Original and the Modified TRAC-P1A with the Data. (BNL Neg. No. 6-1046-80).

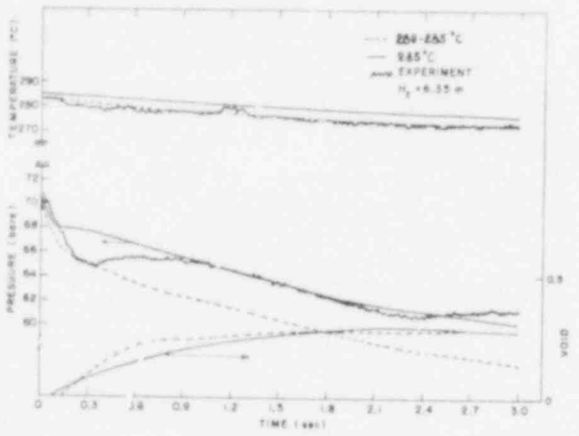

Figure 4.9 Pressure, Temperature, and Voids Time History in a case with the Initial Liquid Temperature Changed. (BNL Neg. No. 7-234-80).

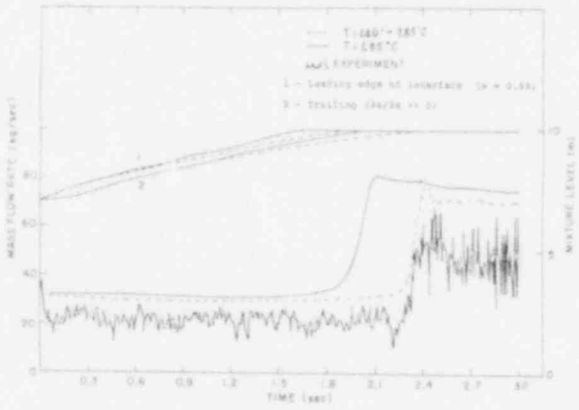

Figure 4.10 Mass Flow rate and Mixture Level Time History in a case with the Initial Liquid Temperature Changed. (BNL Neg. No. 7-233-80).

Based on the test analyzed to date, TRAC performs quite well for the Battelle-Frankfurt top blowdown test and correctly predicts the sequence of the events.

4.6 RPI Phase Separation Tests (U. S. Rohatgi)

In the last quarterly (Rohatgi, 1980b), the RPI Phase Separation Tests 1, 3, 6, and 8 (Lahey, 1978) were discussed. It was found that the tests with two outlets gave stable solution with the right side outlet having more flow than the left side outlet. This discrepancy has been further investigated in this quarter. There are two possible causes; interfacial phenomena or numerics of converting from cylindrical geometry to 2-D slab configuration. Test 8 (with rods) has been run again for air flow only, and the results are shown in Figure 4.11. Here again the solution is stable, but the two outlets have unequal flow, thus discounting the interfacial phenomena as a possible cause. Next an extra column of large cells, 20 m width, was added to the test section. This additional column of cells does not communicate with the main test section. The test section and the TRAC-P1A prediction are shown in Figure 4.12. Here, however, the results are dramatically different. If there were no numerical problem, the results should have remained the same. This information has been transmitted to LASL. The remaining four RPI tests at high inlet quality are being tried to see if higher gas velocity makes any difference. Meanwhile, the causes of nonconvergence in 2-D slab are also being investigated.

4.7 FRIGG-Loop Forced and Natural Circulation Tests (L. Neymotin)

After it had been revealed that the failures to reach a steady-state for the FRIGG Tests with the 3-D as well as with 1-D vessel module were mainly due to some coupling of modelling and numerical problems, efforts were focused on studying more detailed intermediate results during the "steady-state" oscillations. At this point, it seems that neither the conductive heat transfer in the rods nor the rod-to-liquid or two-phase flow heat transfer are responsible for the initiation and development of the observed instabilities. The models for interfacial mass and momentum transfer are being currently studied.

4.8 Improvements in Plotting Package (Y. Sanborn)

The TRAC and PAD* interface program, which provides TRAC-P1A with the versatile plotting capability of PAD has been made available for pipe, break, and vessel components. (Vessel routines are still being tested.) With PAD, TRAC is able to produce the time dependent plots of one or more variables from one or more TRAC runs. Also, similar spatial plots from one or more connected components can be generated. A user may also specify the titles, xy axis labels and legends.

4.9 Other Related Activities (P. Saha, Y. Sanborn, and L. Barello)

At the request of Dr. Y. Y. Hsu of USNRC, sample calculations were performed to estimate the frictional pressure gradient in a PWR hot leg during a

*PAD is a graphic software developed by H. Berry, Applied Mathematics Department, Brookhaven National Laboratory, with A. Aronson and D. Garber, Department of Nuclear Energy, Brookhaven National Laboratory.

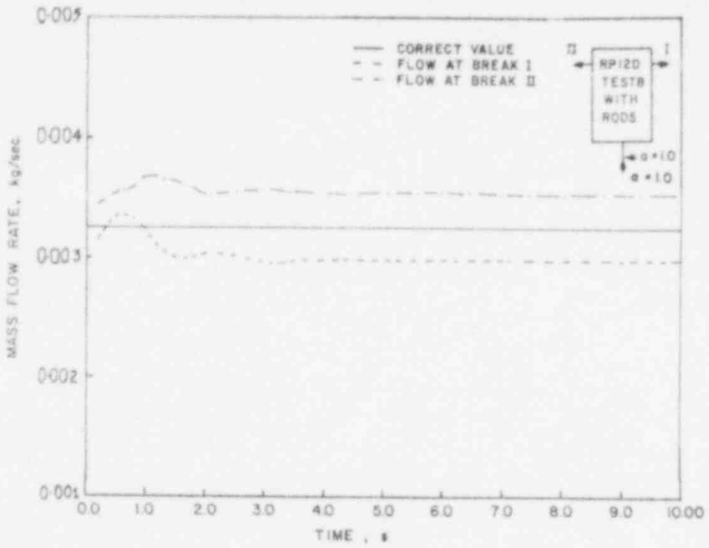

Figure 4.11 Air Flow Rates at the Break as Predicted by TRAC-P1A for RPI Test Section with Rods. (BNL Neg. No. 6-1050-80).

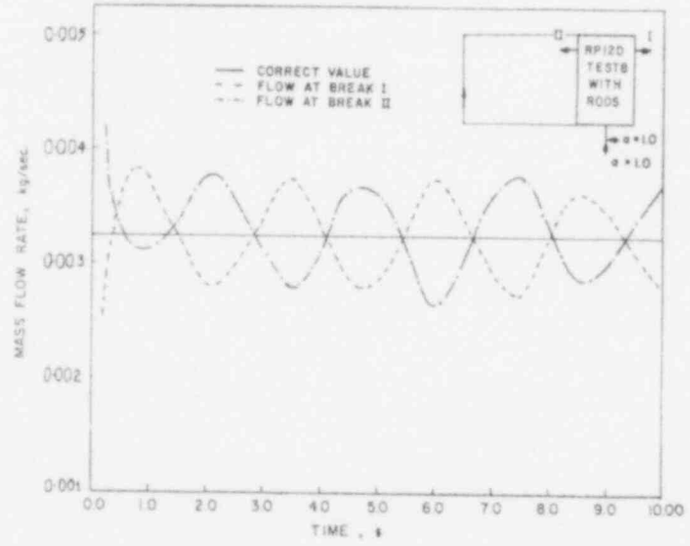

Figure 4.12 Air Flow Rates at the Break as Predicted by TRAC-P1A for Modified RPI Test Section with Rods and an Extra Non-communicating Column with Large Cells. (BNL Neg. No. 6-1042-80,.

small-break LOCA. A parametric study revealed that the magnitude of the pressure gradient would be in the range of 10-100 N/m^2-m. The details of the calculation are being transmitted to Dr. Hsu in a BNL memorandum.

Also, the following papers on TRAC assessment were presented at the recent ANS annual meeting at Las Vegas, Nevada:

1. "Calculation of the CANON Experiment Using the TRAC Code," S. V. Lekach (BNL).
2. "Independent Assessment of TRAC-P1A with Moby-Dick Nitrogen-Water Tests," P. Saha (BNL).

REFERENCES

ALAMGIR, Md. and LIENHARD, J. H., (1980), "Correlation of Pressure Undershoot during Hot-Water Depressurization," to be published in the ASME Journal of Heat Transfer.

DUKLER, A. E. and SMITH, L. (1977), "Two Phase Interactions in Counter Current Flow: Studies of the Flooding Mechanism," NUREG-CR-0617, Annual Report November 1975 - October 1977.

ERICSON, L., et al (1979), "The Marviken Full Scale Critical Flow Tests," MXC-225, September 1979, Joint Reactor Safety Experiments in the Marviken Power Station, Sweden.

ERICSON, L., et al (1979), "The Marviken Full Scale Critical Flow Tests," MXC-226, September 1979, Joint Reactor Safety Experiments in the Marviken Power Station, Sweden.

HOLZER, B., KANZLEITER, T., and STEINHOFF, F., (1977), "Determination of Water Level and Phase Separation Effects During the Initial Blowdown Phase," Battelle-Institute of Frankfurt (Main), February 1977.

JEANDEY, C., and BARRIERE, G., (1979), "Partie I, Etude Experimentale d'Ecoulements Eau-Air a Grande Vittese," DTCE/STT/SERTE Note T.T. No. 599, Janvier 1979.

LAHEY, R. T., (1978), "Two-Phase Flow Phenomena in Nuclear Reactor Technology," Quarterly Progress Report 8, March - May 1978, NUREG-CR-0418, 1978.

RIEGEL, B., (1979), "Experience Super-CANON," TT/SETRE/79-2-B/BR.

ROHATGI, U. S., (1980a), "Marviken Critical Flow Tests," in WRSRD Quarterly Progress Report, Reactor Safety Research Program, January - March 1980, BNL-NUREG-51218, June 1980.

ROHATGI, U. S., (1980b), "RPI Phase Separation Tests," in WRSRD Quarterly Progress Report, Reactor Safety Research Program, January - March 1980, BNL-NUREG-51218, June 1980.

SAHA, P., (1980), "Moby-Dick Nitrogen-Water Experiments," in WRSRD Quarterly Progress Report, Reactor Safety Research Program, January - March 1980, BNL-NUREG-51218, June 1980.

II. METALLURGY AND MATERIALS EVALUATION

SUMMARY

The effects of service related variables on the stress corrosion cracking of Inconel 600 steam generator tubing are being determined experimentally and the data used to formulate a model for service life expectancy.

U-bend type specimens exposures have been completed at several temperatures in several environments. Continuing tests included both U-bend and localized dent specimens. The presence of carbon steel in one test has accelerated the failure time of several heats of Inconel 600 and supported observations made by other investigators.

Crack initiation times for material slowly strained in a constant extension rate test have been determined and applied as a correction to previously reported data. The effect of cold work on one heat of material has been determined.

A comparison of constant stress and cyclic stress loading of specimens shows that the cyclic component has little effect on the failure times for the frequencies tested.

1. Stress Corrosion Cracking of PWR Steam Generator Tubing

(T.S. Bulischeck and D. van Rooyen)

Laboratory investigations are continuing to expand and refine the data base for the model to predict the service life expectancy of Inconel 600 steam generator tubing. The effects of stress, strain, strain rate, temperature and environment on mill annealed and sensitized material are being studied.

1.1 Constant Deflection Tests

Reverse tube U-bend specimens and localized dent specimens are providing crack initiation data in several environments at several temperatures. Exposures with U-bend specimens are completed in pure water at 365°C and 345°C, primary water at 365°C and 345°C, and in AVT at 345°C. The material was tested in the as received or pickled condition and failure times for the replicate specimens agreed reasonably well.

Recent tests in pure H_2O at 365°C containing both U-bend and localized dent specimens showed a marked change in the failure times of some of the susceptible materials previously tested under the same conditions. The dented specimens are constructed by inserting a 2" length of steam generator tubing into a carbon steel block with essentially zero clearance between the outer wall of the tube and the hole in the block. A screw in the side of the block is used to force a ball into the side of the tubing to produce dents of 5, 20 or 40 mils. Several low carbon Alloy 600 heats which had average failure times of 10 to 14 weeks without carbon steel in the system now had 4 out of 4 specimens from each heat fail in less than three weeks. This supports the observations made by Coriou that coupling Inconel 600 to carbon steel shifts the potential and decreases the failure time. Dented specimens have not produced any failures at this time.

Pure water exposures at 325°C and 290°C and AVT tests at 325°C are continuing.

1.2 Constant Extension Rate Tests (CERT)

Plate type tensile specimens prepared from tubing that has been carefully rolled flat to minimize wall reduction have been used for the initial determination of crack velocities as a function of temperatures. Three heats of material tested over a temperature range of 290°C to 365°C had activation energies of 42 Kcal/mole. This number is currently being refined by determining the precise time at which initiation occurs in slowly strained specimens, together with the effect of cold work.

Initially the crack velocities were calculated by assuming that initiation started at the yield point of the material and the intergranular crack depth was divided by the straining time between this point and final fracture. A series of tests have been completed where the specimens were strained for various times, then removed from test and destructively examined to determine the depth of intergranular penetration. Extrapolation of the crack depth data to zero crack depth gives the initiation time as shown in Figure 1. The strain at which initiation takes place is dependent on the strain rate, and initiation can occur very near the yield point of the material if the strain rate is sufficiently low.

Tubing has been tested in the as received condition, flattened into plate, and with 10% or 40% additional cold reduction to determine the effect of cold work on the crack velocities. Figure 2 shows that while flattening the tubing into plate increases the crack velocity at a given temperature by a factor of 2, further cold working did not have any significant effect. Material with 40% cold work exhibited brittle fracture at very low strains and several additional tests at lower strain rates will be carried out to allow sufficient time for IGSCC to propagate. The crack velocity versus temperature relationships for a low carbon heat of material which was rolled into plate is shown in Figure 3. Corrections have been made for the initiation times at the various temperatures. The effect of cold work will be compensated for after the initiation times for the as received material is compared to that of the plate specimens.

1.3 Constant Stress Tests

Tests completed for one low carbon material in 365°C pure water indicate that the failure time is proportional to σ^{-3}. These specimens required less than 10 days to produce failures when stressed to $\leq$13 Ksi above yield. Susceptible material with the highest carbon content (.05%) has been in test four months at stresses $\leq$27 Ksi above yield without any failures.

1.4 Cyclic Stress Tests

Cyclic stress effects have been examined in the frequency range of 10^{0} to 10^{-3} Hz with load ranges of 90%-110% Y.S. or 110%-130% Y.S. Figure 4 compares the results of constant and cyclic loads applied to a .01% carbon material. The cyclic component has no effect on the failure time which appears to be controlled more by the lowest stress than either the mean or high stress level.

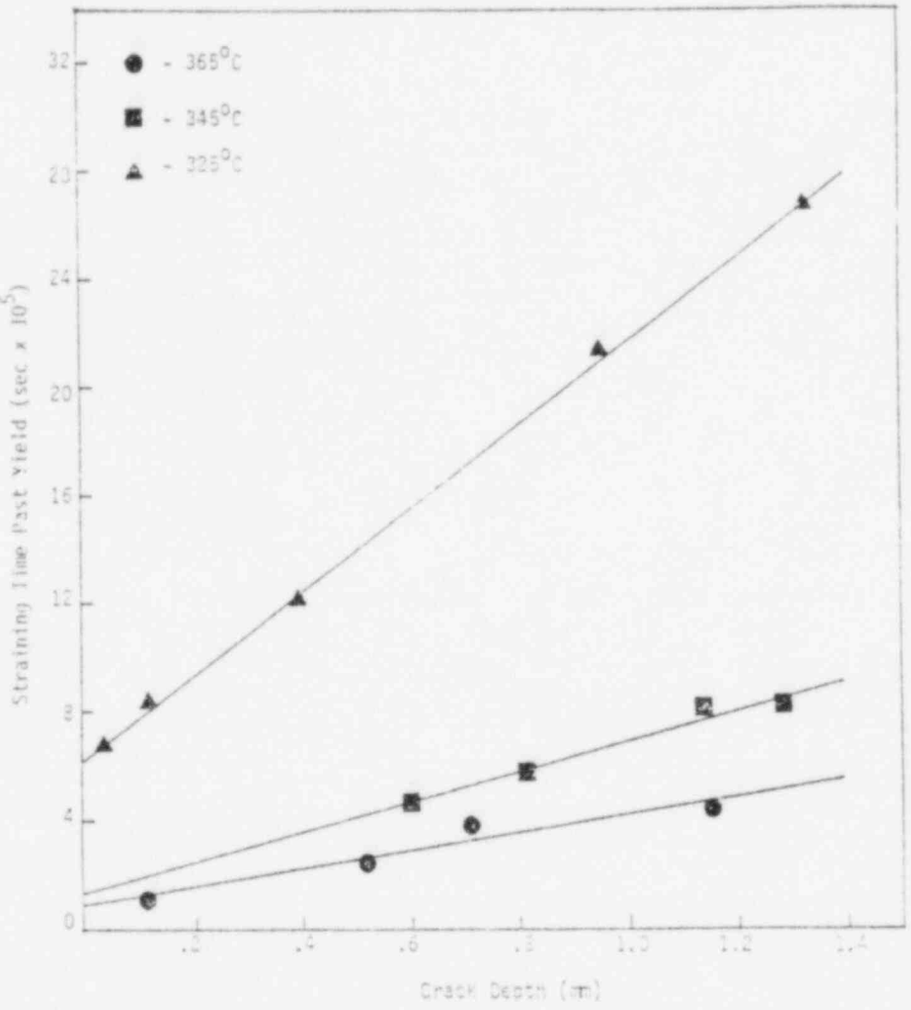

Figure 1 Determination of crack initiation for Inconel 600 (.01%C) slowly strained in pure water

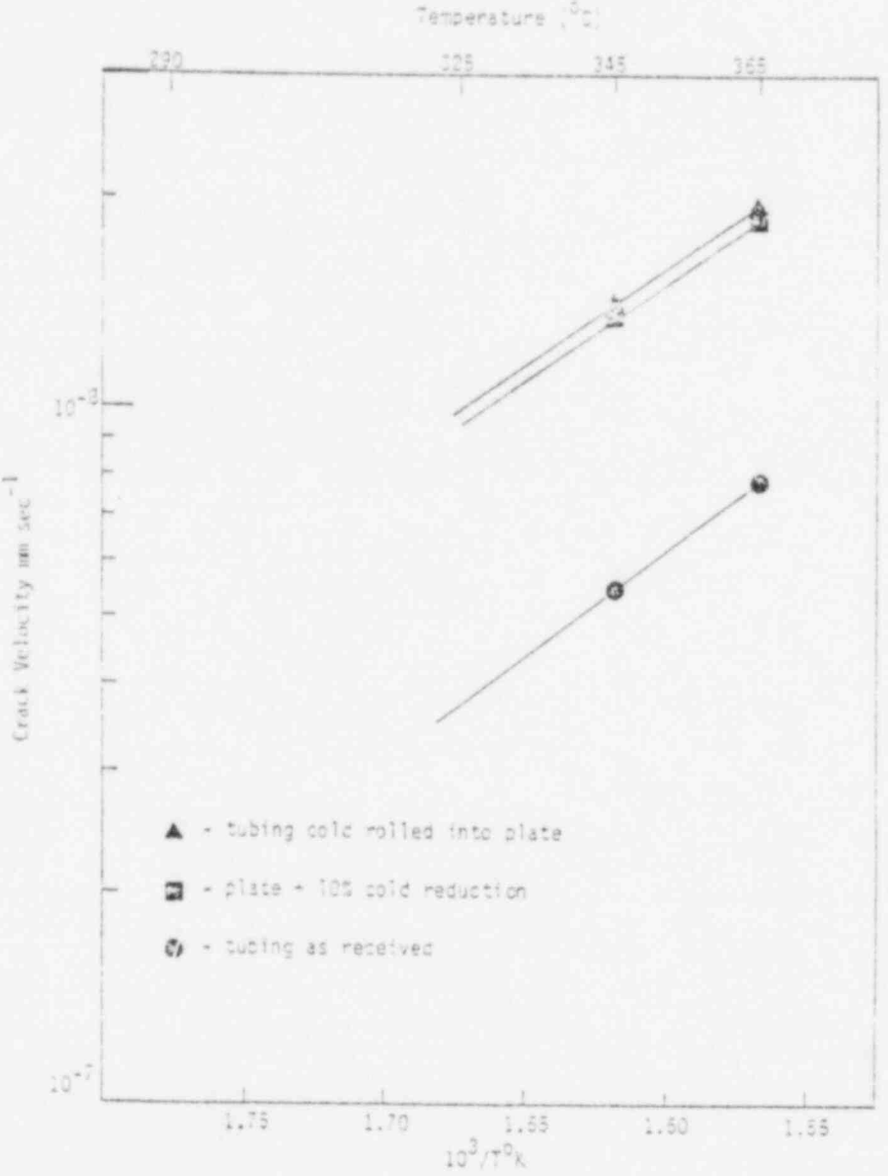

Figure 2 Effect of cold working on crack velocity

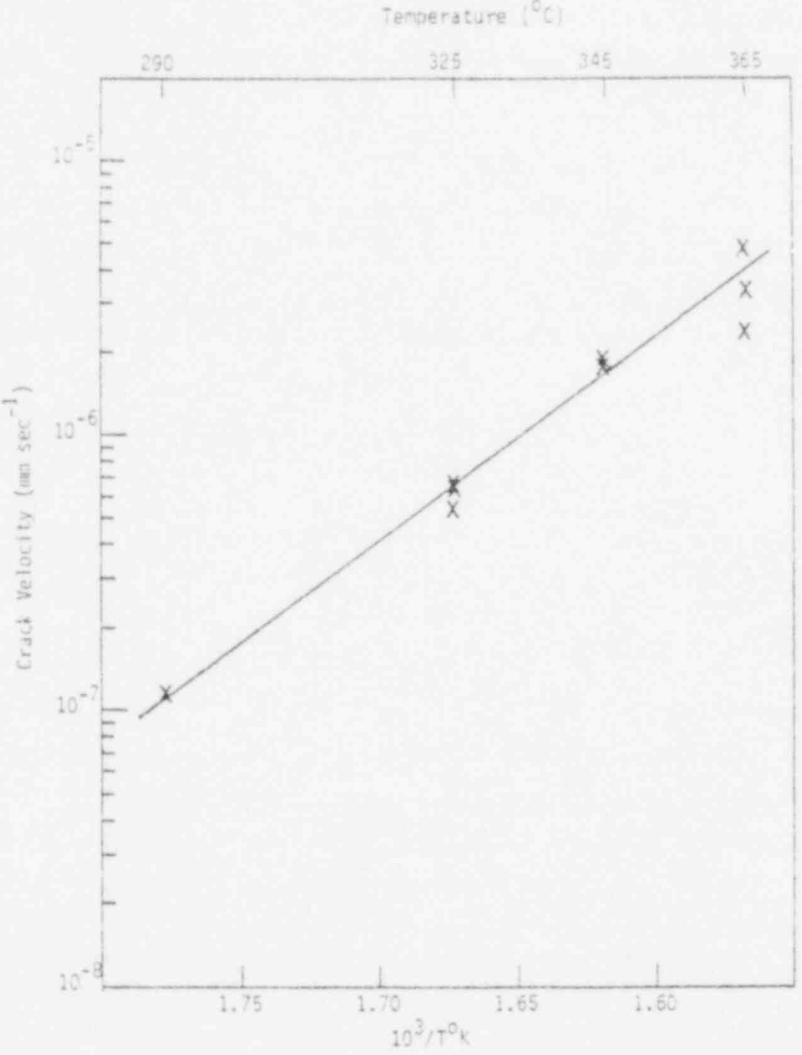

Figure 3 Crack velocities for low carbon (.01%) Inconel 600 slowly strained in CERT after correcting for crack initiation times

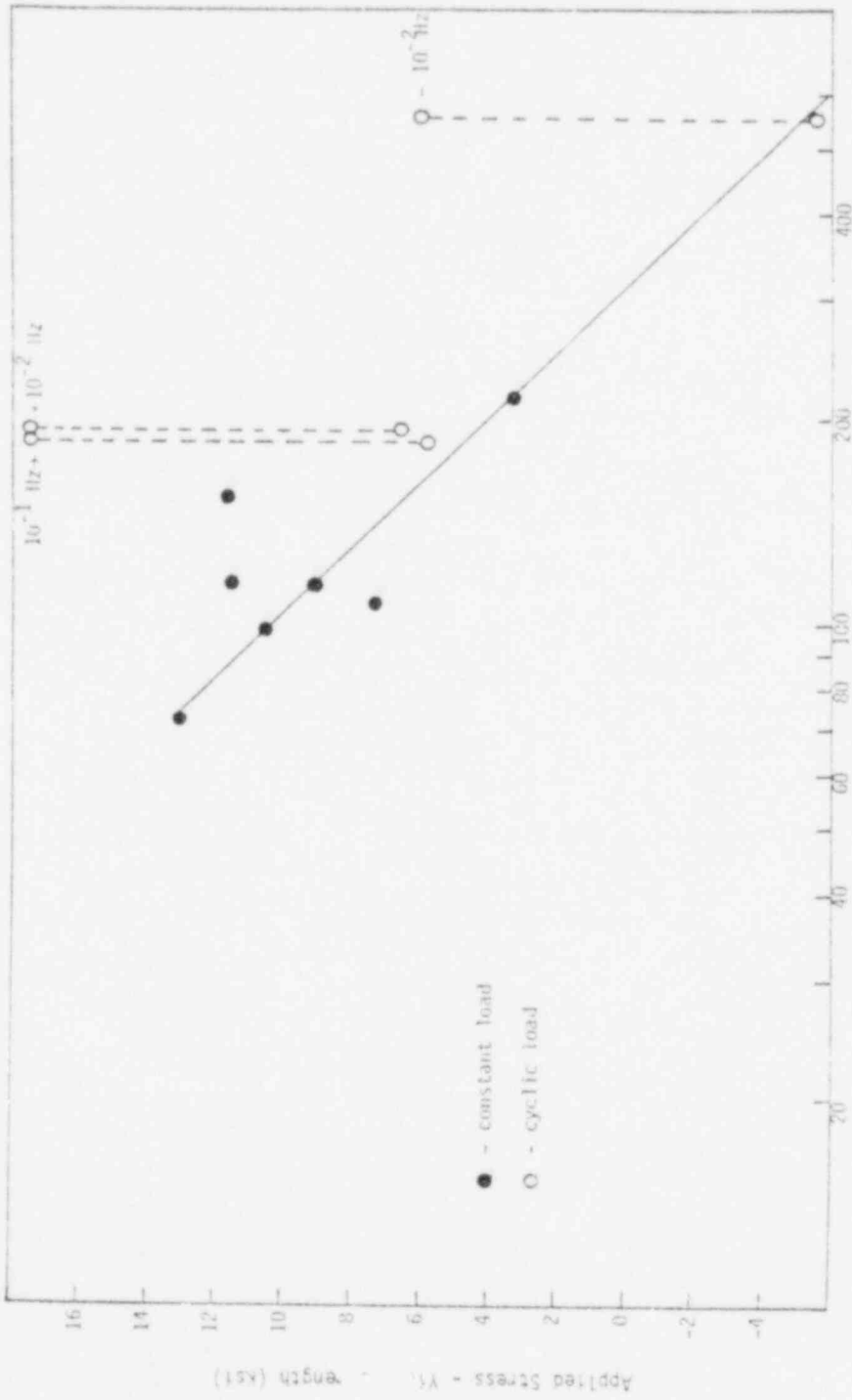

Figure 4 Comparison of Constant Load and Cyclic Load Tests in 365°C D.I. H_2O